CZECH TECHNICAL UNIVERSITY IN PRAGUE

Faculty of Nuclear Sciences and Physical Engineering

Department of Physics

Diploma Thesis

Design and optimization of the optical readout system for electromagnetic calorimeter FOCAL

Miroslav Šimko

Supervisor: Doc. RNDr. Vojtěch Petráček CSc.

Prague, 2013

ČESKÉ UČENÍ TECHNICKÉ
V PRAZE
Fakulta Jaderná a Fyzikálně Inženýrská
Katedra fyziky

Diplomová práce

Návrh a optimalizace optického vyčítacího systému elektromagnetického kalorimetru FOCAL

Miroslav Šimko

Vedoucí práce: Doc. RNDr. Vojtěch Petráček CSc.

Praha, 2013

Prohlášení:

Prohlašuji, že jsem svou diplomovou práci vypracoval samostatně a použil jsem pouze podklady (literaturu, projekty, software, atd.) uvedené v přiloženém seznamu.

Nemám závažný důvod proti užití tohoto školního díla ve smyslu § 60 Zákona č. 121/2000 Sb., o právu autorském, o právech souvisejících s právem autorským a o změně některých zákonů (autorský zákon).

V Praze dne 30.7.2013 Miroslav Šimko

Title:
Design and optimization of the optical readout system for electromagnetic calorimeter FOCAL

Author: Miroslav Šimko

Specialization: Experimental nuclear and partical physics

Supervisor: Doc. RNDr. Vojtčh Petráček CSc.
Consultant: RNDr. Petr Chaloupka, Ph.D.

Abstract:
The thesis consists of two separate parts: The first one describes the interventions to the Detector Control System (DCS) for the Silicon Drift Detector (SDD) during the time period from September 2012 until July 2013; The second one discuses the scintillator design concept of the currently developed electromagnetic forward calorimeter FoCal.

Because the first long shutdown of the LHC is currently under way, some interventions to the SDD DCS, that would be otherwise impossible, were accomplished because the detector is not running. The changes done to the DCS concern humidity sensors and the high voltage supply. In addition, one of the DCS computers and a cable swap were repaired.

A design concept of FoCal calorimeter, that employs scintillators as the detection medium, is being developed by Czech Technical University in Prague. This concept uses optical fibers to read out the optical information from the scintillator pads. This optical readout is thoroughly examined in this thesis.

In order to test the readout, a probing station was built. Moreover, several samples of the scintillator pads were tested.

Key words:
ALICE, FoCal, optical readout, scintillator, electromagnetic calorimeter, control system, DCS, ITS, SDD

Název práce:
Návrh a optimalizace optického vyčítacího systému elektromagnetického kalorimetru FOCAL

Autor: Miroslav Šimko

Abstrakt:
Práce se skládá ze dvou oddělených částí, z nichž se první zabývá změnami, které byly provedeny na řídícím systému (DCS) pro křemíkový driftový detektor (SDD) od září 2012 do července 2013. Druhá část se zabývá konceptem pro právě vyvíjený dopředný elektromagnetický kalorimetr FoCal s využitím scintilátorů pro detekci. Tento koncept se právě vyvíjí na ČVUT v Praze.

Protože v roce 2013 probíhá na LHC první dlouhá odstávka „Long Shutdown" (LS1), bylo možné provést na DCS některé změny, které by jinak nebyly proveditelné, kdyby detektor běžel. Změny vytvořené na DCS se týkají senzorů vlhkosti a řízení zdrojů vysokého napětí. Navíc byl nahrazen nefunkční počítač pro DCS a odstraněn problém s vyměněnými kabely.

Náš koncept FoCalu se scintilačními detektory používá pro vyčítání optického signálu ze scintilačních padů optická vlákna. Tento způsob vyčítání je v práci důkladně prozkoumán.

Aby mohlo být vyčítání scintilačních padů otestováno, sestavili jsme zkoušecí stanici. Navíc byla odezva z několika vzorků scintilačních padů změřena.

Klíčová slova:
ALICE, FoCal, optické vyčítání, scintilátor, elektromagnetický kalorimetr, řídící systém, DCS, ITS, SDD, PVSS

Acknowledgement

I would like to thank Doc. RNDr. Vojtěch Petráček CSc., and especially RNDr. Petr Chaloupka, Ph.D. for their consultation and help with the laboratory work. I would also like to thank Roman Lavička for his kind disposal of the results of the readout simulations.

Contents

Chapter 1

Introduction

This thesis describes my work for the ALICE experiment at CERN and it consists of two separate parts: The first part describes the interventions to the Detector Control System of the Silicon Drift Detector and ends with Chapter 6; The second part discuses the scintillator design concept of the currently developed ALICE Forward Detector (FoCal) and starts in Chapter 7. Chapter 13 is a conclusion where the results of both parts are discussed.

1.1 Detector Control System for the Silicon Drift Detector

As a part of the service work at ALICE, I work as a Detector Control System (DCS) expert on the Silicon Drift Detector (SDD). This part of the thesis describes the changes done to the SDD DCS during the time period between September 2012 and July 2013 and continues on the work, described in my Bachelor Thesis [87] and Research Project [88].

In 2013, the first long shutdown (LS1) of the LHC is under way. Therefore, most of the interventions were done during this period. Moreover, some changes that would be otherwise impossible could be performed because the detector is not running.

1.2 Scintillator concept of the Forward Calorimeter (FoCal)

The new electromagnetic forward calorimeter FoCal is currently being developed at ALICE. A design concept, where scintillators are employed as the detection medium, is proposed by Czech Technical University.

The optical signal from the scintillators is read out via optical fibers, in this design. This thesis focuses on the optical readout of the scintillator pads and the means of its testing.

Chapter 2

The ALICE experiment

2.1 Overview

ALICE (A Large Ion Collider Experiment) is a versatile particle detector system built at the LHC (Large Hadron Collider) at the CERN (Centre Européenne pour Recherche Nucléaire (European Organization for Nuclear Research)) experimental facility. It was designed [1,4] with the purpose of studying broad range of observables in the collisions of ultra-relativistic heavy ion collisions as well as in collision of protons both of which are available at LHC collider.

The physics aim [2, 3] of the experiment is to study quantum chromodynamics (QCD), the strong interaction sector of the standard model. The main goal of the ALICE is to study physical properties of the quark gluon plasma (QGP), possibly a state of strongly interacting matter that existed a few microseconds after the beginning of the universe.

The detector was built by a collaboration including over 1000 physicists and engineers from 105 institutes in 30 countries, and is composed of 18 sub-detectors and their associated supply systems [1, 4]. Figure 2.1 summarizes the layout of ALICE. The table 2.1 shows details of the position of the detectors, and also the acceptance in pseudorapidity[1] η and the azimuthal angle ϕ.

The central part of the detector is barrel shaped and is situated in a solenoid magnet which is reused from the L3 experiment at LEP. The L3 magnet provides magnetic field of 0.5 T. From inside out, the barrel consists of Inner Tracking System (ITS), of six planes of high-resolution silicon pixel (SPD), drift (SDD), and strip (SSD) detectors, a cylindrical Time-Projection Chamber (TPC), three particle identification arrays of Time-of-Flight (TOF), Ring Imaging Cherenkov (HMPID) and Transition Radiation (TRD) detectors, and two electromagnetic calorimeters (PHOS and EMCal). All the sub-detectors except HMPID, PHOS, and EMCal cover the full azimuth.

In one forward direction the, so called, muon arm is placed, consisting of several absorbers, a dipole magnet, and fourteen planes of triggering and tracking chambers.

[1] Pseudo-rapidity, quantity approximately equal to rapidity, is defined

$$\eta = -\ln\tan\frac{\theta}{2}\,,$$

where θ is the longitudinal angle.

Table 2.1: Summary of the ALICE detector [1]. The acceptance in η is calculated from the interaction point. The position is the approximate distance from the interaction point to the face of the detector and corresponds to the radius of the barrel detectors.

Detector	Acceptance (η, ϕ)	Position [m]	Dimension [m^2]
ITS layer 1,2 (SPD)	± 2, ± 1.4	0.039, 0.076	0.21
ITS layer 3,4 (SDD)	± 0.9, ± 0.9	0.150, 0.239	1.31
ITS layer 5,6 (SSD)	± 0.97, ± 0.97	0.380, 0.430	5.0
TPC	± 0.9 at r=2.8 m	0.848, 2.466	readout 32.5 m^2
	± 1.5 at r=1.4 m		Vol. 90 m^3
TRD	± 0.84	2.90, 3.68	716
TOF	± 0.9	3.78	141
HMPID	± 0.6, $1.2° < \phi < 58.8°$	5.0	11
PHOS	± 0.12, $220° < \phi < 320°$	4.6	8.6
EMCal	± 0.7, $80° < \phi < 187°$	4.36	44
ACORDE	± 1.3, $60° < \phi < 60°$	8.5	43
Muon Spectrometer			
Tracking station 1	$-2.5 < \eta < -4.0$	-5.36	4.7
Tracking station 2		-6.86	7.9
Tracking station 3		-9.83	14.4
Tracking station 4		-12.92	26.5
Tracking station 5		-14.22	41.8
Trigger station 1	$-2.5 < \eta < -4.0$	-16.12	64.6
Trigger station 2		-17.12	73.1
ZDC:ZN	$\lvert\eta\rvert < 8.8$	± 116	2×0.0049
ZDC:ZP	$6.5 < \lvert\eta\rvert < 7.5$	± 116	2×0.027
	$-9.7° < \phi < 9.7°$		
ZDC:ZEM	$4.8 < \eta < 5.7$,	7.25	2×0.0049
	$-16° < \phi < 16°$ and		
	$164° < \phi < 196°$		
PMD	$2.3 < \eta < 3.7$	3.64	2.59
FMD disc 1	$3.62 < \eta < 5.03$	inner: 3.2	
FMD disc 2	$1.7 < \eta < 3.68$	inner: 0.834	0.266
		outer: 0.752	
FMD disc 3	$-3.4 < \eta < -1.7$	inner: -0.628	
		outer: -0752	
V0A	$2.8 < \eta < 5.1$	3.4	0.548
V0C	$-1.7 < \eta < -3.7$	-0.897	0.315
T0A	$4.61 < \eta < 4.92$	3.75	0.0038
T0C	$-3.28 < \eta < -2.97$	-0.727	0.0038

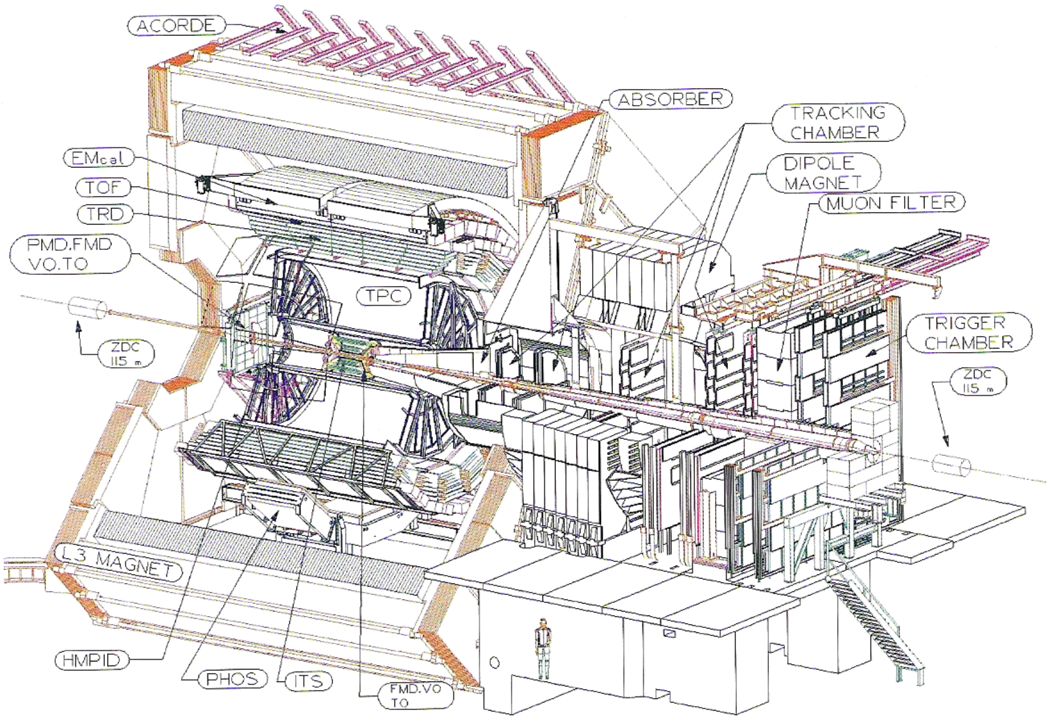

Figure 2.1: Overview of the ALICE detector [1].

What is more, there are several smaller detectors situated in smaller angles (ZDC, PMD, FMD, T0, V0). Furthermore, an array of scintilators (ACORDE) is used for triggering of cosmic rays.

The detector is designed to withstand the highest multiplicities anticipated for Pb-Pb collisions. The design of ALICE was optimized for the value of approximately $\mathrm{d}N/\mathrm{d}\eta = 4000$, but tested for simulations exceeding twice that amount. The radiation environment in the detector was simulated for the planned run scenario. Runs with p-p, low- and high-mass ion-ion collisions for over a ten year period were assumed. Moreover, beam-beam and beam-gas interactions, and miss-injected beams were expected as additional radiation source. Table 2.2 shows doses and neutron fluences for the central detectors.

2.2 Beam pipe

Since one part of work presented in this thesis is connected to Inner Tracking System and the second part of a forward calorimeter the properties of the beam pipe are of interest as they significantly influence precision of the particle tracking and momentum resolution of these detectors.

The interface between the LHC machine and the ALICE experiment is represented by the beam vacuum system [1, 4]. The coating of the beam pipe must be, therefore, transparent for the traversing high energy particles but also prevent the gas from leaking inside the vacuum chamber.

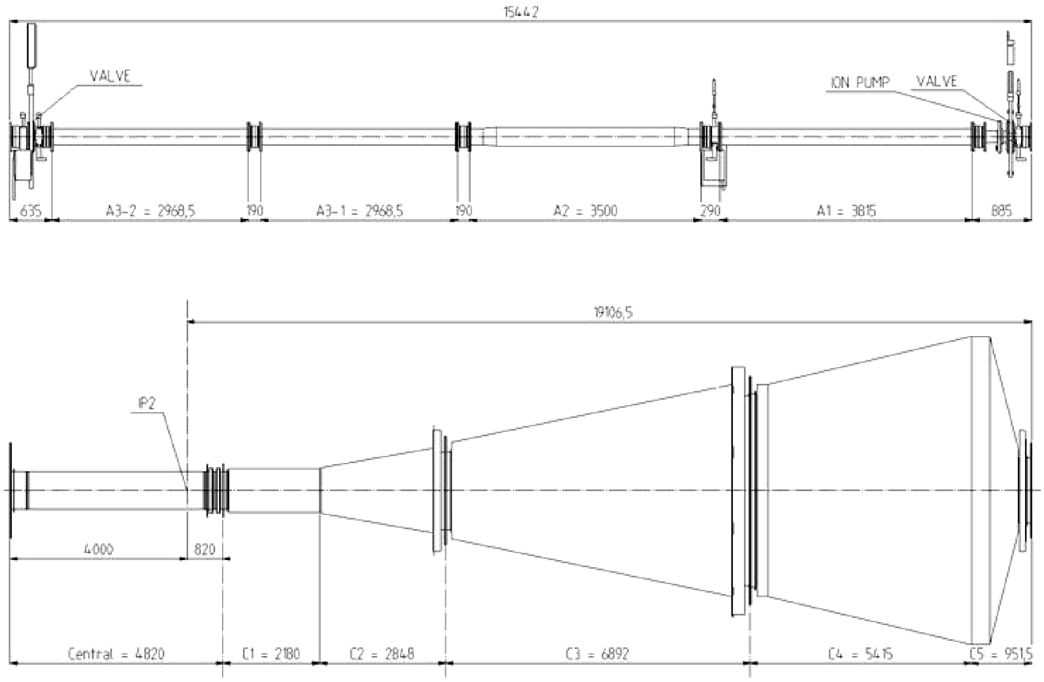

Figure 2.2: Layout of the ALICE vacuum chamber [1].

The vacuum system is pumped via a combination of a combination of lumped sputter-ion and distributed Non-Evaporable Getter (NEG) pumps. The NEG system is made of thin sputtered coating along the whole surface of the vacuum chambers.

Table 2.2: Doses and neutron fluences in central detectors [22].

System	Radius (cm)	Dose (Gy)	h-Φ (cm^{-2}) 1 MeV n-equ
SPD1	3.9	2.7×10^3	3.5×10^{12}
SPD2	7.6	6.8×10^2	1.3×10^{12}
SDD1	14	2.5×10^2	5.5×10^{11}
SDD2	24	1.2×10^2	3.2×10^{11}
SSD1	40	5.0×10^1	2.3×10^{11}
SSD2	45	3.0×10^1	2.0×10^{11}
TPC(in)	78	1.6×10^1	1.5×10^{11}
TPC(out)	278	2.2×10^0	4.5×10^{10}
TRD	320	1.8×10^0	2.6×10^{10}
TOF	350	1.2×10^0	2.0×10^{10}
PHOS	460	5.0×10^{-1}	1.7×10^{10}
HMPID	460	5.0×10^{-1}	1.7×10^{10}

Table 2.3: Dimensions and materials of the ALICE vacuum chamber [1].

Name	Length [mm]	min. ID [mm]	max. ID [mm]	Material
A/1	3815	80	80	Copper
A/2	3500	60	96	Copper oval chamber
A/3-1	2968.5	80	80	Copper
A/3-2	2968.5	80	80	Copper
Central	4800	58	58	Beryllium, Stainless steel
C/1	2180	58	58	Stainless steel
C/2	2848	58	120	Stainless steel
C/3	6892	120	300	Stainless steel
C/4	5415	300	450	Stainless steel
C/5	951.5	100	450	Stainless steel

The ALICE beam pipes extend 19 m to both sides of the IP (see Fig. 2.2) and consist of 3 sections. The Central section is a 4 m long beryllium pipe, protected by a polyimide wrapping about 80 μm thick, and ranges between -3585 mm $< z <$ 365 mm. The characteristics of the beam pipes are summarized in Table 2.3.

Chapter 3

The Inner Tracking System (ITS)

3.1 Overview

The Inner Tracking System (ITS) [1, 4, 7] is the closest detector system to the beam pipe. Its main purposes are to localize the primary vertex and the secondary vertexes with a resolution better than 100 μm, to track and identify particles with momentum below 200 MeV, to improve the momentum and angle resolution of the TPC and to reconstruct particles that traverse dead regions of the TPC. The ITS also provides mechanical support for the beam pipe so it does not move during operation.

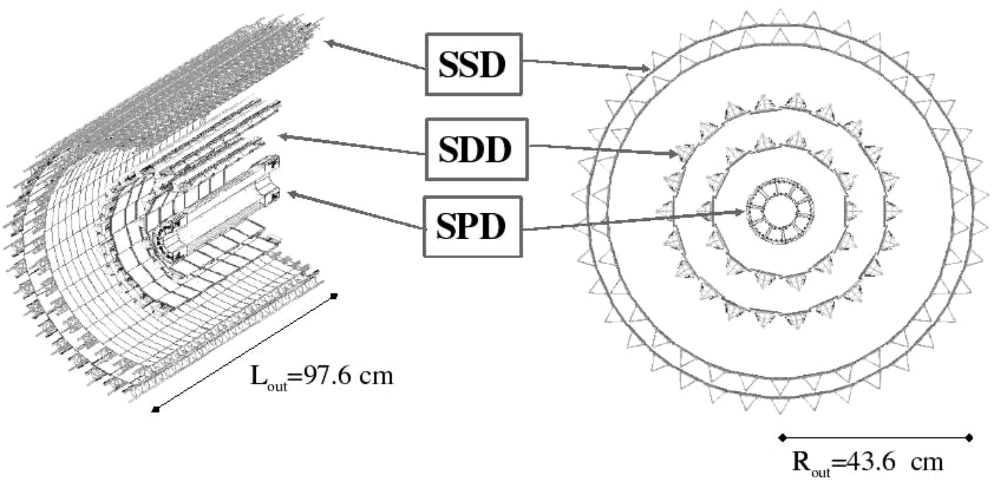

Figure 3.1: Layout of the ITS [1].

The ITS consists of six cylindrical layers of silicon detectors, coaxial with the beam pipe, as shown schematically in Figure 3.1. It is located in radii between 4 and 43 cm, and covers the pseudorapidity range of $|\eta| < 0.9$. The innermost layer of silicon pixel detector (SPD) has extended pseudorapidity coverage ($|\eta| < 1.98$) to provide, together with the FMD, continuous coverage for the measurement of the charged particles multiplicity. The dimensions of all the ITS detectors are summarized in Table 3.1.

Table 3.1: Dimensions of the ITS detectors (active areas) [7].

Layer	Type	r [cm]	$\pm z$ [cm]	Area [m^2]	Channels
1	pixel	3.9	14.1	0.07	3 276 800
2	pixel	7.6	14.1	0.14	6 553 600
3	drift	15.0	22.2	0.42	43 008
4	drift	23.9	29.7	0.89	90 112
5	strip	38.0	43.1	2.20	1 148 928
6	strip	43.0	48.9	2.80	1 495 200
Total area				6.28	

Because of the high particle density estimated in ion collisions at LHC (as many as 50 particles per cm^2 have been predicted for the innermost layer), and due to the fact that high resolution of the impact parameter is required, Silicon Pixel Detectors (SPD) have been chosen for the innermost two layers, and Silicon Drift Detectors (SDD) for the following two layers. Double sided Silicon micro-Strip Detectors (SSD) were installed on the two outer layers where the track density is expected to be below one particle per cm^2. The main parameters for each of the three detector types are shown in Table 3.2. The detectors and front-end electronics are held by lightweight carbon-fiber structure (Figure 3.2).

The four outer layers are equipped with analogue readout and can, therefore, be used for particle identification via dE/dx measurement in the non-relativistic ($1/\beta^2$) region. This feature gives the ITS stand-alone capacity as a low-p_{T} particle spectrometer.

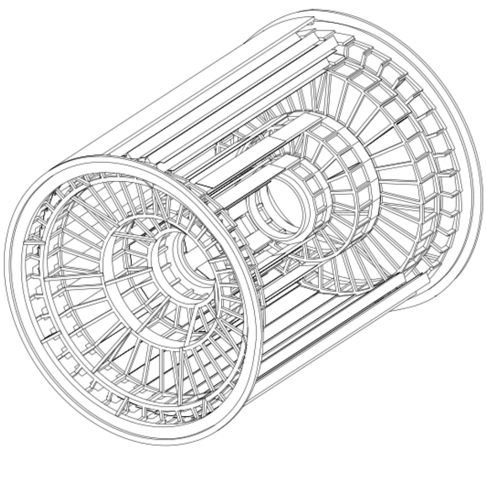

Figure 3.2: Schematic view of the mechanical support of the ITS [4].

The granularity of the detectors was designed to cope with a track density of

Table 3.2: Parameters of the three detector types used in ITS [1]. A module represents a single sensor element. The maximum occupancy is calculated for the central Pb-Pb collisions.

Parameter		Silicon Pixel	Silicon Drift	Silicon Strip
Spatial precision $r\phi$	[μm]	12	35	20
Spatial precision z	[μm]	100	25	830
Two track resolution $r\phi$	[μm]	100	200	300
Two track resolution z	[μm]	850	600	2400
Cell size	[μm^2]	50×425	202×294	95×40000
Active area per module	[mm^2]	12.8×69.6	72.5×75.3	73×40
Readout channels per module		40960	2×256	2×768
Total number of modules		240	260	1698
Total number of readout channels	[k]	9835	133	2608
Total number of cells	[M]	9.84	23	2.6
Max. occupancy (inner layer)	[%]	2.1	2.5	4
Max. occupancy (outer layer)	[%]	0.6	1.0	3.3
Power dissipation in barrel	[W]	1350	1060	850
Power dissipation in end-cap	[W]	30	1750	1150

dN/dη = 8000, the upper limit of theoretical predictions. With this track density, the ITS would detect more than 15 000 tracks. The ITS detectors have a spatial resolution of the order of a few tens of μm, with the precision of 12 μm for the detectors closest to the primary vertex. They, therefore, provide a resolution on the impact-parameter measurement adequate for heavy-flavored particle detection. The resolution is better than 60 μm in the $r\phi$ plane for $p_{\mathrm{T}} > 1$ GeV/c). The spatial precision of the ITS is a crucial element of the momentum resolution for momenta above 3 GeV/c.

Table 3.3: ITS material budget traversed by straight tracks perpendicularly to the detector surface [1]. Units are percentages of radiation length.

Detector	Pixel		Drift		Strip	
	Inner	Outer	Inner	Outer	Inner	Outer
Layer	1.14	1.14	1.13	1.26	0.83	0.86
Thermal shield/Support		0.52	0.25		0.53	
Total	7.18 (7.26 including air)					

The momentum and impact parameter resolution for low-momentum particles are dominated by multiple scattering effects in the material of the detector. However, the amount of material in densities for drifts and strips must have a minimum thickness of about 300 μm to be able to provide acceptable signal-to-noise ratio.

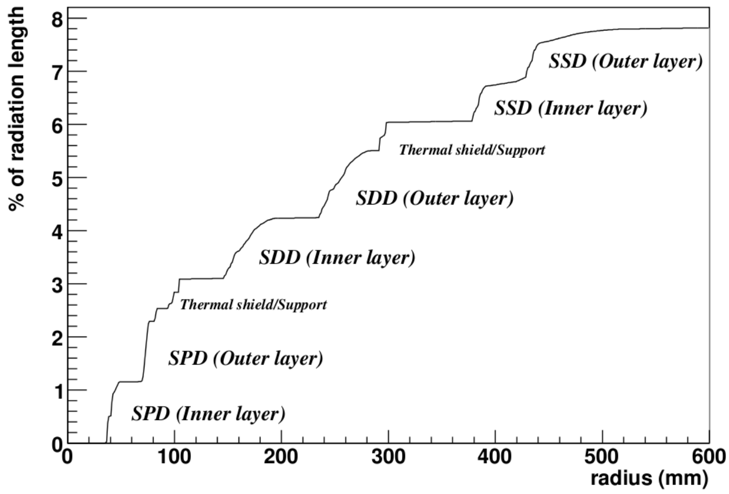

Figure 3.3: Plot of the integral of material thickness traversed by a perpendicular track originating at the primary vertex versus radius [1].

In addition, the detectors must overlap to avoid the existence of dead regions in the detector. The additional material in the active volume (i.e. electronics, cabling, support structure and cooling system) has been designed at comparable effective thickness (Table 3.3 and Figure 3.3).

For the ITS, the total dose expected during operation varies from tens of Gy for the outer parts to about 2.7 kGy for the inner parts (see Table 2.2 in section 2.1). All components of the ITS were tested for their radiation hardness to levels exceeding significantly the anticipated doses. The ITS is designed to withstand ten years of activity in the radiation environment.

Next, we briefly describe SPD and SSD layers. The SDD will be described in more detail in chapter 4 because it is one of the main topics of this thesis.

3.2 Silicon Pixel Detector (SPD)

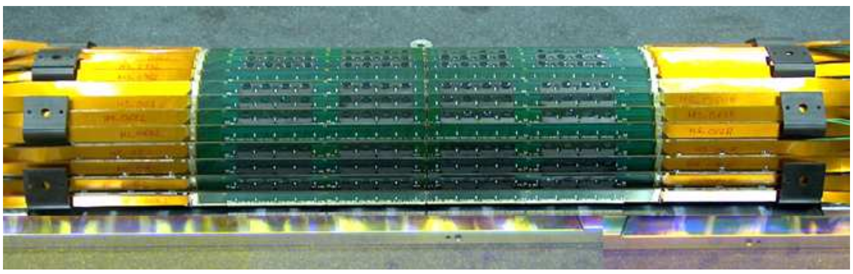

Figure 3.4: Half barrel of the SPD assembled on a reference table [1].

The Silicon Pixel Detector (SPD) composes the two innermost layers of the ITS.

It operates in the region where the track density can reach 50 cm^{-2}, and in relatively high radiation levels: for the inner layer, the total dose in ten year standard running scenario and fluence are estimated to be ≈2.7 kGy and ≈3.5 $\times 10^{12}$ n/cm^2 (1 MeV neutron equivalent), respectively. The SPD is designed to minimize its material budget. The average material traversed by a straight track perpendicular to the detector surface is ≈1% of X_0 per layer.

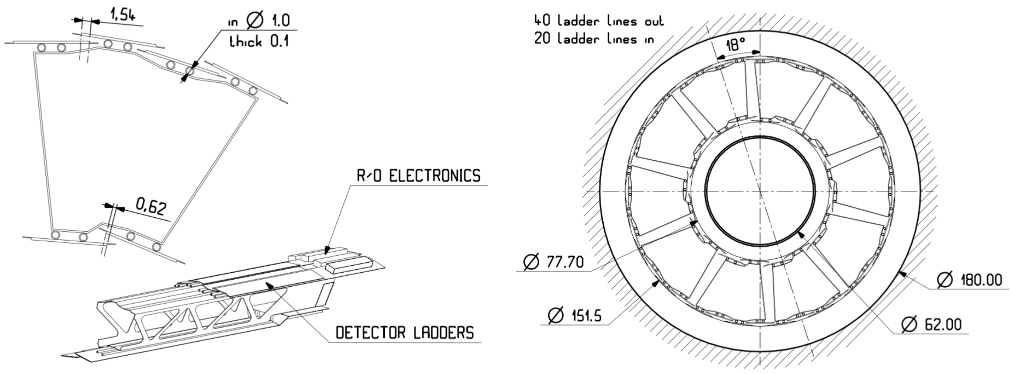

Figure 3.5: Left: view of a sector of the pixel barrel; right: cross-section of the pixel barrel [4].

The SPD is based on hybrid silicon pixels, consisting of two-dimensional matrix (sensor ladder) of reverse-biased silicon detector diodes bump-bonded to readout chips [27]. The readout is binary: the digital output level changes when a signal reaches a set threshold. The basic detector module is called half-stave. Each half-stave consists of two ladders and one readout chip (one Multi-Chip Module, MCM, and one high density aluminium/polyimide multi-layer interconnect). Each ladder is composed of a silicon sensor matrix bump-bonded to 5 front-end chips. The sensor matrix includes 256 × 160 cells measuring 50 μm ($r\phi$) by 425 μm (z).

Two half-staves are attached head-to-head along the z direction to a carbon-fiber support sector. Each sector supports six staves: two on the inner layer and four on the outer layer (see Figure 3.5). In total, the SPD (60 staves) consists of 240 ladders with 1200 chips for a total of 9.8×10^6 cells.

The power generated by the front-end electronics is ≈1.35 kW. The cooling system is of the evaporate type and is based on C_4F_{10}. In addition, the SPD barrel is surrounded by an Al-coated external shield to prevent heat radiation towards the SDD layers.

3.3 Silicon Strip Detector (SSD)

The Silicon Strip Detector (SSD) composes the two outermost layers of the ITS. Those layers are essential for matching of tracks from the TPC to the ITS. Moreover, they provide dE/dx information to assist particle identification for low-momentum particles. The particle density is estimated to be below 0.5 cm^{-2}. Beam tests have shown that the spatial resolution is better than 20 μm in the $r\phi$ direction and 820 μm in the z direction.

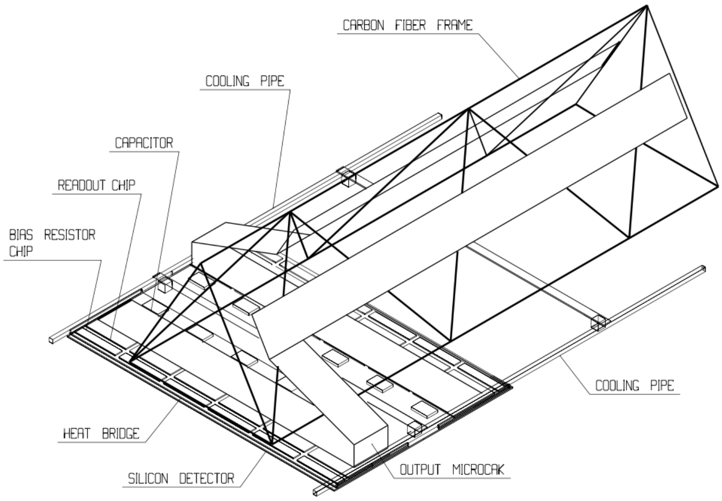

Figure 3.6: 3D view of one SSD module. The module shown here is glued on the carbon fiber ladder support [4].

Both layers use double sided SSDs, which have been chosen, because they introduce less material in the active area, compared to the single-sided SSDs. The detection modules are composed of one sector connected to two hybrids, one on the p-side and one on the n-side of the strips. All interconnections between the sensor and the electronics are made of aluminium on polyimide cables (micro-cables). The modules are assembled in ladders (Figure 3.6), one module wide and up to 25 modules long. The 72 ladders, composed of 1698 modules, are mounted on a mechanical support structure in two concentric cylinders. For each layer, the ladders are mounted in two sightly different radii so they cover the full azimuth.

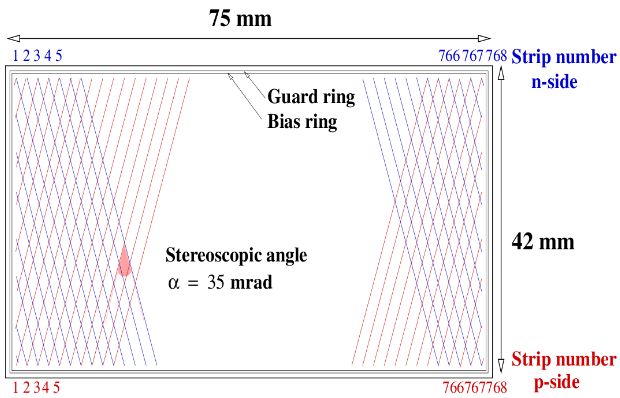

Figure 3.7: Scheme of a part of the SSD. Some characteristic dimensions are indicated [7].

The sensors are 300 μm thick and have 768 strips on each side with a pitch of

95 μm. The stereoscopic angle is 35 mrad (see Figure 3.7) which is a compromise between stereo view and reduction of ambiguities from high particle densities. The sensors are mounted with strips nearly parallel to the magnetic field in order to optimize the resolution in bending direction.

The mechanical support structure is made of carbon fiber composite, thus reducing the material budget. The average power dissipated in the barrel is $\approx$2.2 kW. The cooling system is also designed to introduce minimum material, and to agree with the zero heat balance required for all ALICE detectors. Water was chosen as the cooling medium.

Chapter 4

Silicon Drift Detector (SDD)

4.1 Overview

The Silicon Drift Detectors (SDD) [1, 7, 26] make the two intermediate layers of the ITS in which the particle density is expected to reach 7 cm^{-2}. They were chosen for their very good multi-track capability and because they provide, along with the silicon strip layers, two out of four dE/dx samples needed for the ITS particle identification.

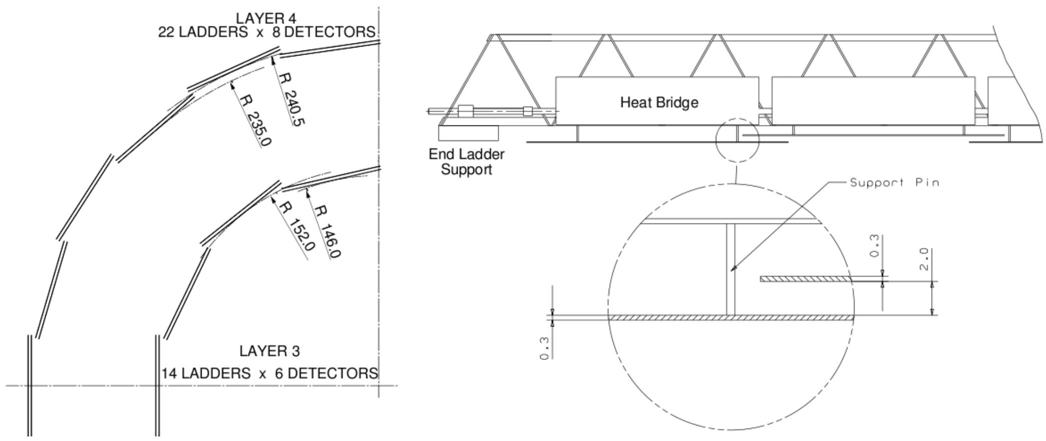

Figure 4.1: Schematic view of the SDD layers [1]. The SDD modules are mounted at different radii at both z and $r\phi$ planes to obtain the full coverage in the acceptance region.

In the drift detectors, the detection is made via measuring the transport time of charge, released during the traversing of a particle at a certain spot, and reconstructing (in one dimension) this spot. The SDDs provide very high resolution at the cost of the readout speed (a few μs).

The two SDD layers are divided into 260 modules, each consisting of one silicon drift detector and two front-end hybrids, connected to an end-ladder LV board (see Fig. 4.4). The modules are mounted on linear structures called ladders. There are

Table 4.1: Main parameters of the ALICE SDD layers and ladders [1].

	layer 3	layer 4
Detectors per ladder	6	8
Ladders per layer	14	22
Detectors per layer	84	176
Ladder sensitive half-length [cm]	22.16	29.64
Average ladder radius [cm]	15.03	23.91
Ladder space-frame weight [g]	11	15
Weight of ladder components [g]	87	121

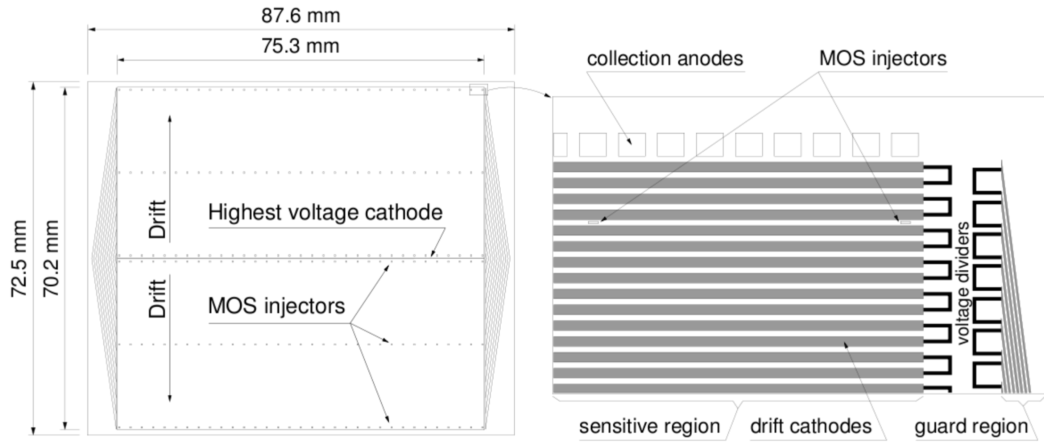

Figure 4.2: Layout of the ALICE SDD [1]. The detecting area is split into two 'drift regions' by the central cathode with the highest voltage. Each drift region has one row of 256 collection anodes and three rows of 33 MOS charge injectors for monitoring the drift velocity. Drift and guard regions have independent voltage dividers.

14 ladders with six modules each on layer 3, and 22 ladders with eight modules each on layer 4. The ladder space frame is made of carbon-fiber reinforced plastic and has a protective coating against humidity. The layout of the SDD layers is shown in Figure 4.1.

The ALICE SDDs were built out of very homogeneous high-resistivity (3 kΩ cm) 300 μm thick Neutron Transmutation Doped (NTD) silicon. As shown in Figure 4.2, the SDDs have a total area of $72.50(r\phi)\times 87.59(z)$ mm^2 and a sensor area of 70.17×75.26 mm^2. The sensitive area is divided into two drift regions by the central cathode strip to which a high-voltage bias of -2.4 kV is applied. A second bias supply of -40 V is added to keep the biasing of the collection independent on the drift voltage. The detector performance, when averaged throughout its whole area, does not depend significantly on the applied bias voltage in a range from -1.65 kV to -2.4 kV, so the bias voltage can be adapted to the specific running conditions.

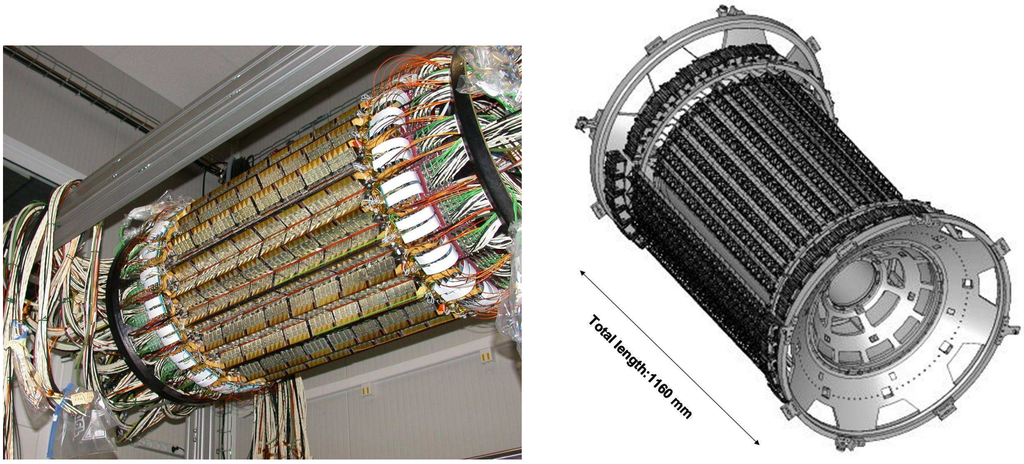

Figure 4.3: Left: the SDD completely assembled, ready to be integrated with the Silicon Strips. Right: A 3D image of the SDD layers, showing the support cones and the ladders of the two layers [1].

The main characteristics of the SDDs are summarized in Tables 4.2, and 3.2 on page 11.

4.2 Calibration

Drift velocity depends on mobility[1] which depends very strongly on temperature ($\mu \propto T^{-2.4}$), thus every module has a different drift speed. The temperature has to be controlled with precision ≈0.1 K.

In order to monitor the drift velocity, so called MOS injectors were installed. They introduce the charge on known positions, thus allowing the drift speed to be measured. Every ≈6 hours (in future this should be improved to ≈10 min during physics runs), special runs take place to calibrate the drift speed [21].

In 2010, however, some of the MOS injectors were destroyed because a beam from LHC crashed near ALICE when the SDDs were turned on. Some changes were made to the detector control so this does not happen again, e.g. the high voltage supplies on the detectors are set to a safe value of 100 V during the time between the measurements [88].

4.3 Power supplies

The two front-end ASICs are connected to the corresponding end-ladder LV boards. The detector bias voltage is provided by specially designed printed circuit, called

[1]Mobility μ characterizes how quickly an electron or a hole can move through a material, when pulled by an electric field. It is defined

$$v_d = \mu E\,,$$

where v_d is the drift velocity and E is the applied electric field.

Table 4.2: The main characteristics of the ALICE silicon drift detectors [1].

Sensitive area	70.17×75.26 mm^2
Total area	72.50×87.59 mm^2
Collection anodes (readout channels)	2×256
Anode pitch	294 μm
Operating voltage	-1.65 to -2.4 kV
Nominal bias of the collection region	-40 V
Drift velocity	5.6 to 8.1 μm/ns
Maximum drift time	4.3 to 6.3 μs
Cell size at drift velocity 8.1 μm/ns	294×202 μm^2
Cells per detector at drift velocity 8.1 μm/ns	$2\times256\times174$
Total number of cells (266 SDDs)	23×10^6
Average resolution along the drift ($r\phi$)	35 μm
Average resolution along the drift (z)	25 μm
Detection efficiency	99.5%
Average double-track resolution at 70% efficiency at max. field	700 μm

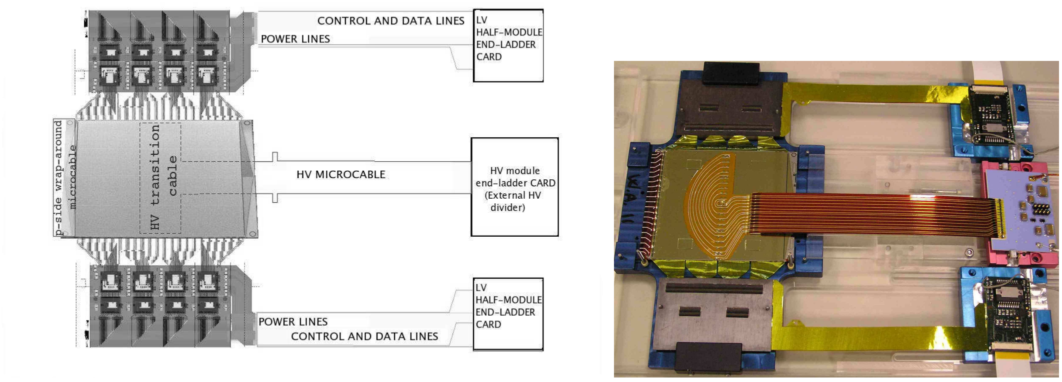

Figure 4.4: Scheme (left) and a photograph (right) of a SDD module [1].

"micro-cables" which can carry high-voltage up to 2.4 kV and connect the detectors to the HV end-ladder boards.

The connections to the central bias cathode and to the injector line are provided by a micro-cable, glued to the p-side. The bias lines are wire bonded to the corresponding bonding pads. The high-voltage is then brought to the n-side using the so called 'wrap-around' cable. These cables are clearly visible in Figure 4.4.

The LV boards ensure the signal interfaces and low-voltage distribution, carry the low-voltage regulators, the circuitry to drive the MOS injectors and the interface with the DCS. The HV boards carry the support high-voltage divider. The end ladder boards are connected to the DCS via mini coaxial cables.

Chapter 5

Detector Control System (DCS)

The main objective of the ALICE Detector Control System (DCS) [8, 9] is to ensure safe and correct operation of the ALICE experiment. It provides remote control in such a way that the whole ALICE experiment can be operated from a single workplace (ALICE Control Room – ACR at LHC point 2). The DCS was designed to reduce the downtime of the experiment, and therefore, contribute to high running efficiency. Although being developed by various groups in parallel, the DCS is a coherent and homogeneous system.

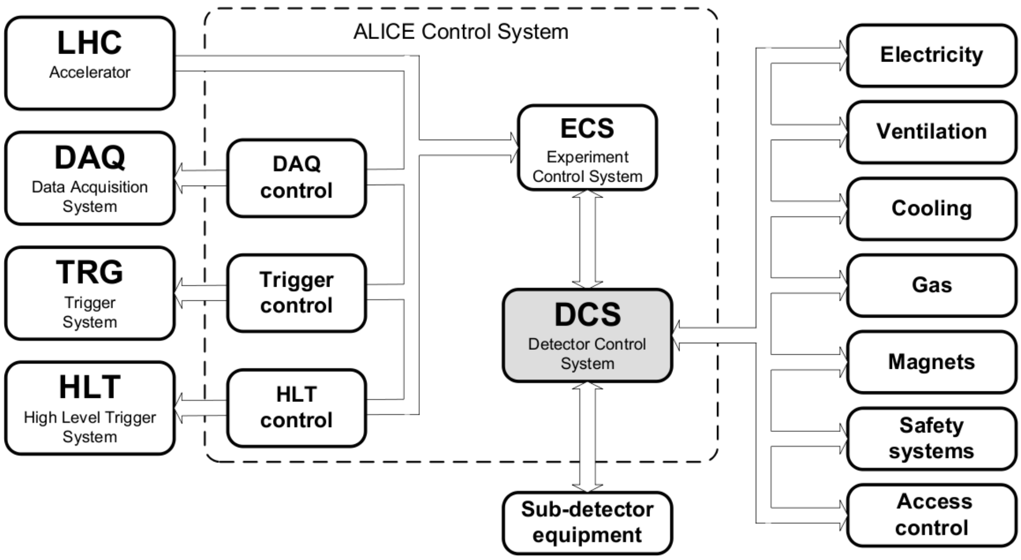

Figure 5.1: The ALICE online systems [8].

The DCS is a part of the ALICE Control System. As shown in figure 5.1, the ALICE Control System includes all control activities in the ALICE experiment: the Experiment Control System (ECS), the DCS, the Data Acquisition (DAQ), the Trigger System (TRG) and the High-Level Trigger (HLT – see [8] or [87]). The DCS takes care of interfering with the various services of the sub-detectors (such as cooling, electricity, magnets, safety, etc.). The ECS is responsible for the synchronization of the various systems, i.e. DCS, DAQ, TRG and HLT.

5.1 Hardware architecture

The hardware architecture is divided into three layers (see figure 5.2). The 'supervisory layer' is composed of PCs that provide user interfaces to the operators and are connected to the disk servers (that hold databases, archiving, etc.). The DCS also interferes with external systems through this layer via the DIP protocol (Data Interchange Protocol) which is a protocol defined in CERN that allows exchanging of information between various systems.

The supervisory layer interfaces to the 'control layer' mainly through a LAN. This layer also consists mainly of PCs that interface to the experimental equipment, but also of the PLCs or PLC-like structures. These devices collect information from the lower, so called 'field', layer and make the detector equipment available for the supervisory layer. The control layer interfaces to the equipment in the field layer through fieldbuses, but also via the LAN.

The field layer contains all field devices (such as power supplies, fieldbus nodes, etc.), sensors and actuators, etc. It is designed to avoid sharing of devices between different sub-detectors so they can run simultaneously and concurrently.

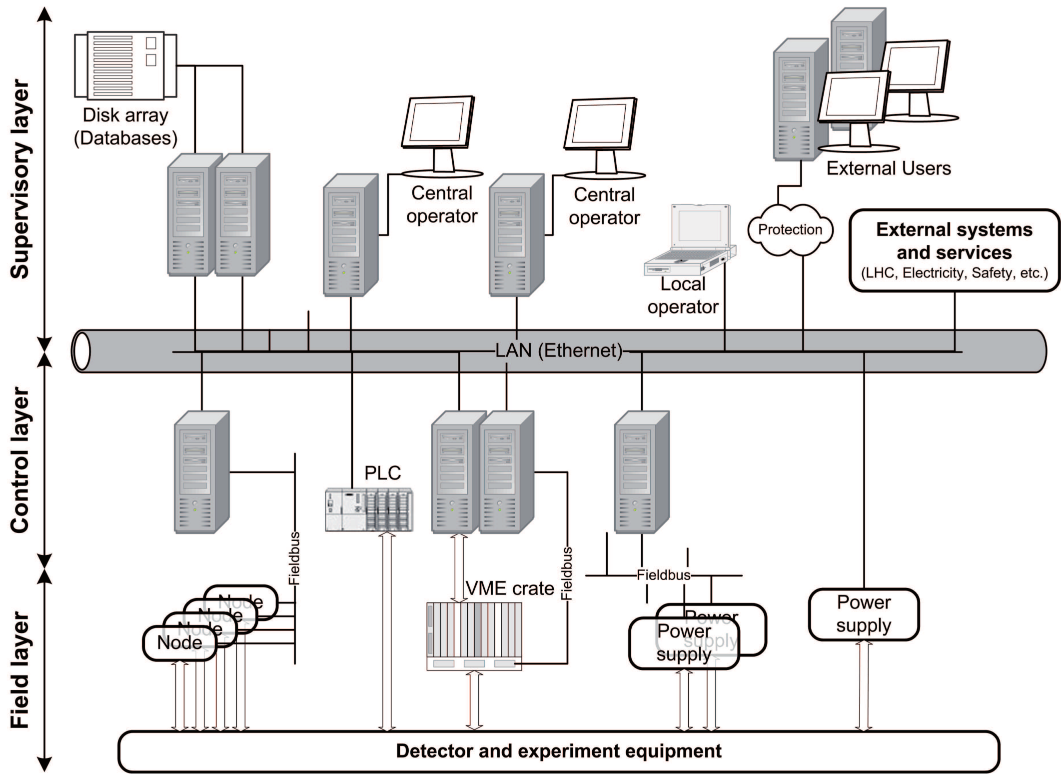

Figure 5.2: DCS hardware architecture [8].

5.2 Software architecture

The core software of the DCS is a commercial SCADA[1] (Supervisory Controls and Data Acquisition) program PVSSII [15].

The control system is built using the 'JCOP framework' which contains Finite State Machine functionality (see bellow), drivers for different types of hardware, communication protocols, and configurable components for frequently used applications such as low voltage power supply, etc. The framework also includes many other utilities such as interfaces to the various databases (configuration, archiving), visualization tools, access control, alarm configuration and reporting, etc. The JCOP framework is being developed by a joint effort between all the LHC experiments.

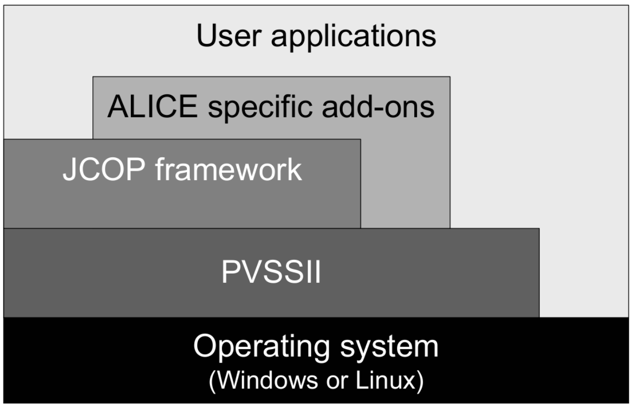

Figure 5.3: Overview of the software layers in the control system [8].

Several add-ons to this framework exist specially for the ALICE specific needs. The various layers are shown in figure 5.3.

PVSSII, the framework and the user applications are designed to work mainly on Microsoft Windows and Linux platforms. Some limitations, however, may exist for some Windows specific features, when using Linux.

5.2.1 Finite State Machine (FSM)

The hierarchical control structure is a tree-like structure composed of, so called, units. The units' behavior is modeled by the Finite State Machine (FSM) [17]. It is an intuitive, generic mechanism to program behavior of a piece of equipment or a sub-system.

There are three types of units: Device Units (DU), Control Units (CU), and Logical Units (LU). The Device Units are units with no children. They take care of a piece of hardware directly. The Logical Units integrate several Device units in a group. Finally, the Control Units are units that have children which may be DUs, LUs, and even CUs.

[1]As the name indicates, SCADA (Supervisory Controls and Data Acquisition) are programs, designed to control and collect data from various hardware devices. They are not meant to be the full control systems, but focus on the supervisory level. As such, they are purely software products positioned on top of the hardware to which they are interfaced via PCs or PLCs [18].

Every object in the FSM has a set of 'states' between which it can switch by performing 'actions'. The states propagate 'up' the FSM tree which means that the parent units react to the change of states of the children units. The actions propagate 'down' the tree so that when the parent unit performs an action the children units react to it (see Fig. 5.4).

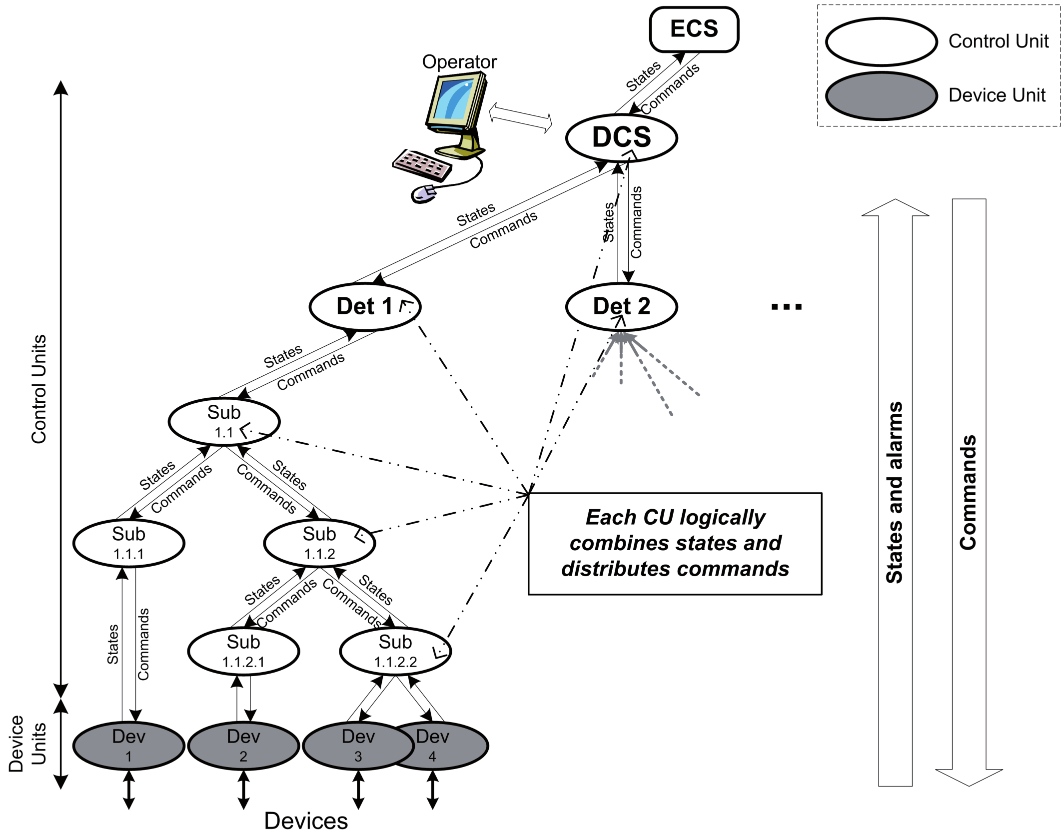

Figure 5.4: DCS hierarchical control architecture [8].

For example, a layer of silicon drift detectors has a state '`READY`' which is defined so that the layer is `READY` when more than 50% of its ladders are `READY`. If more than a half of the layers are in e.g. state '`ERROR`', the layer performs action '`MOVE_ERROR`' and propagates the action to the layers and switches them off. When all of the detectors are in state '`OFF`', the layer moves to state '`OFF`'.

5.2.2 Datapoint concept

The PVSS [11, 16] has its own run-time database, which allows storing data from the hardware devices. This database is designed in such a way that the data are easily accessible and can be treated as variables. Therefore, it has to be optimized for fast access. However, the stored data are difficult for accessing from outside the PVSSII. That is why the JCOP framework also includes an archiving tool.

The device data in the PVSS run-time database are structured as, so called, 'DataPoints' (DP) of their predefined 'DataPoint Types' (DPT). The DPs/DPTs allow to model the devices by defining the DPs' structure. As such, the data associated with a particular device can be grouped together, instead of being held as separate variables. To interfere with the data in the DPs, PVSSII has a special editor called 'PARA'. It is also possible to interfere with them via scripts.

5.2.3 OPC and DIM servers

The OPC (Object Linking and Embedding for Process Control) [11, 19] is a means of controlling a piece of hardware. It provides another abstraction level between hardware and a SCADA system (e.g. PVSS). Therefore, the OPC client works in a similar way as e.g. the drivers on a printer. This is extremely helpful because the developer of a control system does not have to read the registries of HW, etc.

Many vendors of equipment commonly used in the physics experiments provide OPC servers together with their HW. This is the case of CAEN, WIENER and ISEG which is the manufacturer of the SDD high voltage supply.

The OPC servers, although very useful, are quite uneasy to develop. That is why CERN has produced the DIM (Distributed Information Management) protocol [20] which provides a similar abstraction level to the OPC. The PVSS is equipped with a DIM toolkit that helps the developers to connect the equipment to the PVSS datapoints.

Chapter 6

Interventions to the SDD DCS

The first long shutdown of the LHC, called 'LS1', is currently under way in the year 2013. In this chapter, we describe the interventions to the SDD DCS during this shutdown.

6.1 Humidity sensors

In 2011, new humidity sensors were installed inside the SDD volume. To allow the operators to check the humidity values, trends of humidity versus time were implemented [88] so it is possible to check them at any time.

However, one of the sensors showed obviously flawed data so it had to be changed during the LS1. The humidity trend with the wrong values is illustrated in Fig. 6.1. The new sensor will have to be tested with the conditions that will be present when the cooling and ventilation are on.

Supervision of the humidity values are especially important because of the monitoring of the MOS injectors performance (see section 4.2).

6.2 Low voltage cables swap

Accidentally, two cable swaps in the LV channels were found when turning on the SDD chips in 2011. These cables lead to patch panels that control the power supply of the SDD chips. As this problem was not possible to overcome in software, the cables had to be swapped manually. Because when all of the patch panels are turned on, this problem does not affect the performance of the detector, we waited until the LS1 to solve it.

Because the cables split somewhere on the way from the power source to the patch panels, they could not be changed at the LV power supply rack but instead, they had to be swapped in the patch panels inside the L3 magnet. Finally, when the swap was done, the patch panels were tested and they worked properly.

6.3 `alidcscom152` computer crash

In April 2013 one of the DCS computers – `alidcscom152` suddenly crashed. Before we start with the description of the recovery process, some informations about the

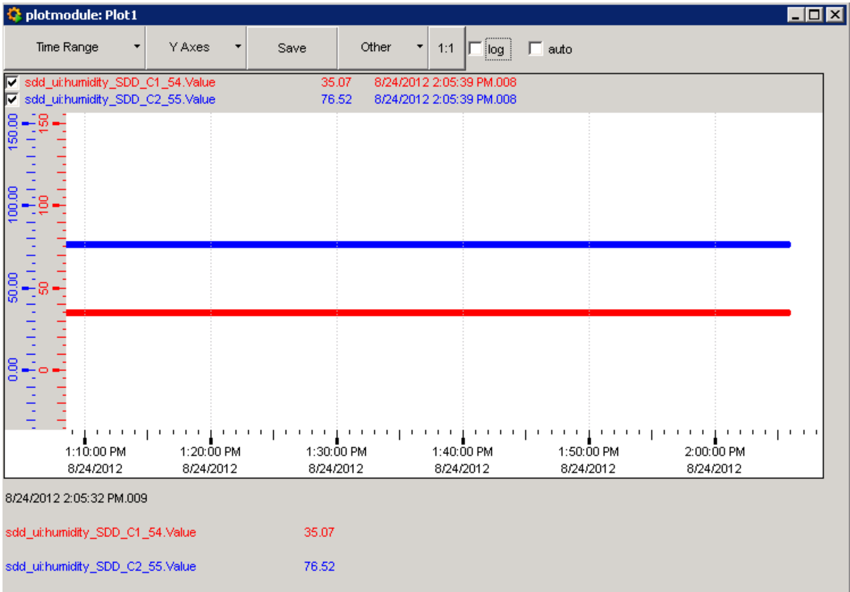

Figure 6.1: Humidity trend with a flawed sensor. Note that one of the sensors show 76.5% humidity.

SDD DCS computers need to be given.

The SDD employs four computers as its DCS servers. Three of them (with the host names `alidcscom817`, `alidcscom818` and `alidcscom820`) were migrated in 2011 [88], and one stayed on the old server (`alidcscom152`). All these servers are accessible from the computer `alidcscom001` that is placed in the CERN network. The properties of the DCS computers are summarized in Tab. 6.1.

Table 6.1: Properties of the SDD DCS computers.

Host name	Operating system	PVSS system
`alidcscom817`	Windows XP	`sdd_ui`
`alidcscom818`	Windows XP	`sdd_dcs`
`alidcscom152`	Windows XP	`sdd_infra`
`alidcscom820`	Linux	no PVSS

Server `alidcscom817`

The `alidcscom817` is dedicated for the user interface of the SDD DCS. This is where the detector is supervised by the operators. The PVSS system on this computer is named `sdd_ui`.

On this computer, all the voltages are being set, the front-end electronics and readout (FERO) are turned on and off, the ventilation and cooling are controlled and humidity and pressure are supervised, everything through a set of UI panels

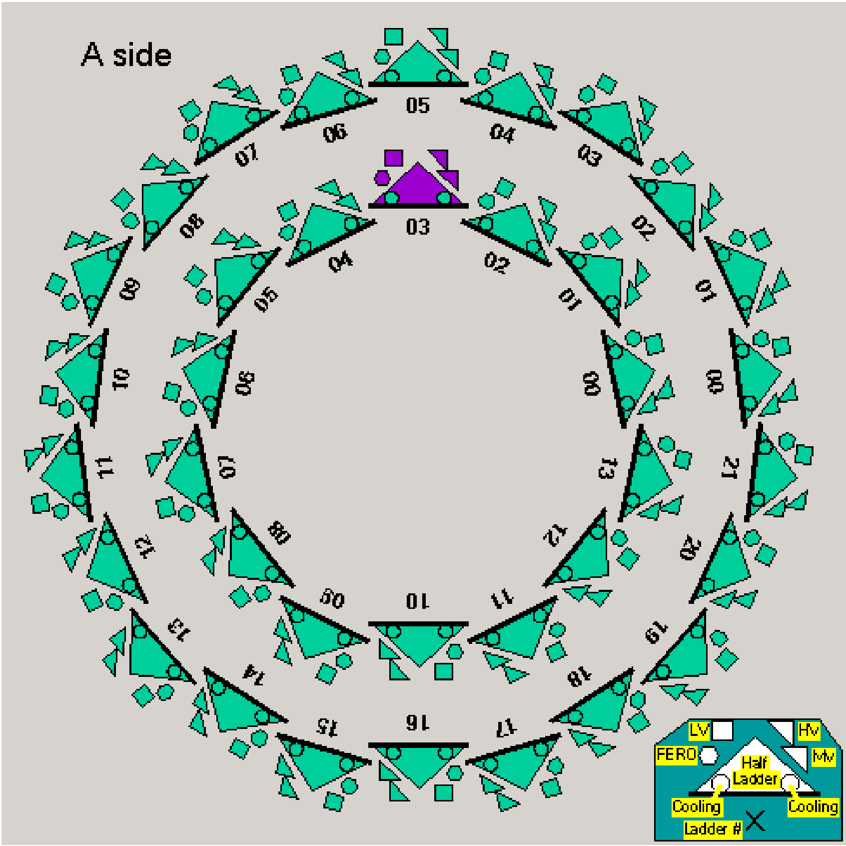

Figure 6.2: A part of the main panel of the SDD DCS user interface on `alidcscom817`, showing all the half-ladders on the A side of the detector (the anti-clockwise side according to the LHC ring).

written in PVSS (an example is in Fig. 6.2). The voltages, pressure and humidity values are drawn into trending plots, also accessible from this server.

A lot of effort is being spent so that almost everything is being supervised on `alidcscom817`, however the automatic control is done by other computers.

Server `alidcscom818`

On this server, the control of the low voltage (LV), cooling and ventilation (CaV) takes place. The PVSS system on `alidcscom818` is named `sdd_dcs`.

Server `alidcscom152`

On server `alidcscom152`, the system `sdd_infra` (for infrastructure) is placed. This computer controls the high voltages. Moreover, the OPC server was installed here. The OPC communicates with the HV supply via a CAN bus from this computer. This computer was the only one that was not migrated because the CAN buses were connected to the PCI interface which was no longer available on the new computers.

Server `alidcscom820`

This is the only computer with Linux operating system which allows the SDD's DIM server to be run here.

6.3.1 New computer

A new computer had to be installed instead of the old `alidcscom152`. This computer still has the PCI interface. Moreover, the IP address, as well as the host name '`alidcscom152`' stayed the same. PVSS and the OPC server had to be installed again. Also, we had to restore all of the old PVSS projects.

6.4 Interventions to the high voltage control

HV power supply crates by the ISEG company are employed at the SDD and are controlled by the `alidcscom152` via two CAN bus interfaces. However, some problems with their control occurred.

6.4.1 Wrong output voltage set

The output voltage of the HV power supplies was slightly different from the set value. In many cases, the value was overshot which created a lot of error messages for the DCS shifter to handle.

This is mitigated in software [88] by first setting the tension values slightly lower ($\sim$ 25 V), and than the value is gradually adjusted until the desired voltage is achieved.

Recently, the power supply racks have been replaced. However, the new racks will have to be tested. We are currently waiting until cooling and ventilation are running.

6.4.2 Dumping of commands

When too many commands are sent to the power supply racks, they start to dump some of them. This problem became more pronounced shortly before the `alidcscom152` crashed. This is particularly dangerous because in some cases there might be a difference of more than 2 kV on the neighboring modules.

Tests showed that this could be caused by the PCI – CAN bus interfaces because less commands are dumped on the crates that are connected to one bus than another. A new computer with USB – CAN buses installed has been prepared to be tested. Whether this overcomes the problem, is currently under investigation. It will have to be tested when the cooling and ventilation are ready.

Chapter 7

Calorimetry

Calorimetry by definition refers to the destructive detection of an incident particle [23, 25, 30, 31]. Conceptually, a calorimeter is a detector which has sufficient thickness so an intercepting particle deposits all its energy in the calorimeter's volume. The particle does so in a cascade or 'shower' of increasingly lower-energy particles which has to be detected so that it leaves information about the original particle's energy.

7.1 Electromagnetic calorimetry

7.1.1 Electromagnetic cascade

The electromagnetic cascade [23,30] can be fully described by the quantum electrodynamics (QED). Because the cascading depends essentially on electron density, it is possible to describe the dimensions of the EMC in a material-independent way, expressed in terms of radiation length X_0. It is defined by the equation:

$$(\Delta E/\Delta x)_{\text{radiation}}\,[X_0^{-1}] = -E\,, \tag{7.1}$$

and can be approximated by

$$X_0\,[\mathrm{g/cm^2}] \approx 180A/Z^2 \quad \text{(to better than 20\% for} \approx Z > 13).$$

Above the energy of approximately 1 GeV, the principal energy loss mechanisms (electron–positron pair production for photons and Bremsstralung for positrons and electrons) become more or less energy independent in terms of radiation lengths (see Figures 7.2 and 7.1). Through these processes the electromagnetic cascade (EMC) propagates.

Lets consider a high energy electron or positron that hits a block of material. This particle will first emit a Bremstrahlung photon. If the energy of the Bremstrahlung photon is high enough, it will, consequently, create an electron-positron pair that Bremstrahlungs again, etc (note that the EMC started by a photon starts with an electron positron pair production).

The shower progresses with exponential growth until the secondary particles are no longer capable of multiplying. While the high-energy part of the EMC is characterized by X_0, the low-energy part is governed by 'the critical energy ϵ' of the

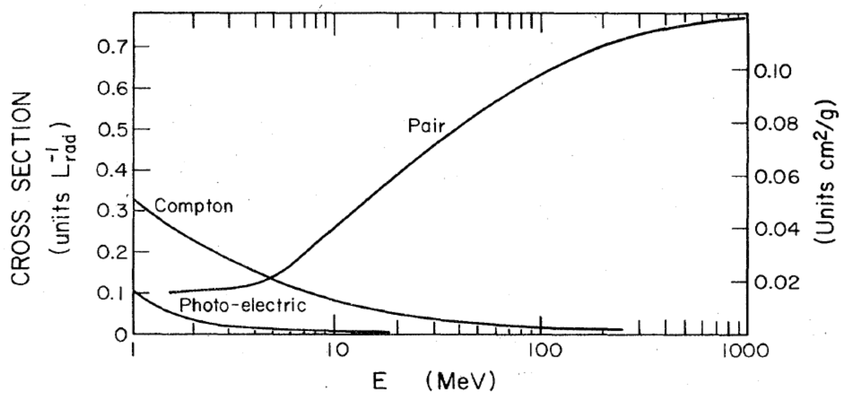

Figure 7.1: Photon cross-section in lead as a function of photon energy. The cross-section is shown in terms of radiation length (left y–ordinate) and per g/cm^2 (right y–ordinate) [5].

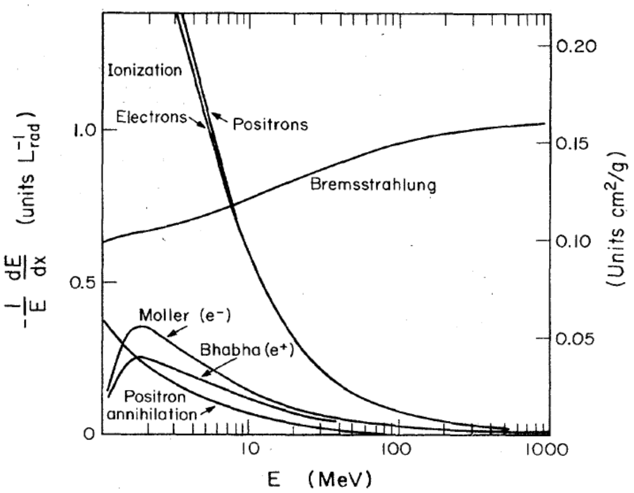

Figure 7.2: Fractional energy loss of electrons and positrons in lead as a function of energy [5].

medium. It is defined as energy lost in *collisions* by electrons or positrons of energy ϵ, i.e.

$$(\mathrm{d}E/\mathrm{d}x)_{\text{collisions}}\,[X_0^{-1}] = -\epsilon\,, \quad \text{where } \epsilon\,[\text{MeV}] \approx 550 \times Z^{-1} \tag{7.2}$$

(accurate to better than 10% for $Z > 13$). The critical energy ϵ defines the dividing line between the shower multiplication and the subsequent dissipation of the EMC through ionization and excitation.

The analytical description of the EMC longitudinal energy profile has been given in the prescription [34]:

$$\mathrm{d}E/\mathrm{d}t = E_0 b^{\alpha+1}/\Gamma(\alpha+1) t^{\alpha} \mathrm{e}^{-bt}, \tag{7.3}$$

where $t = x/X_0$, $\alpha = bt_{\max}$, and $b \approx 0.5$; the symbol $\Gamma()$ stands for the gamma

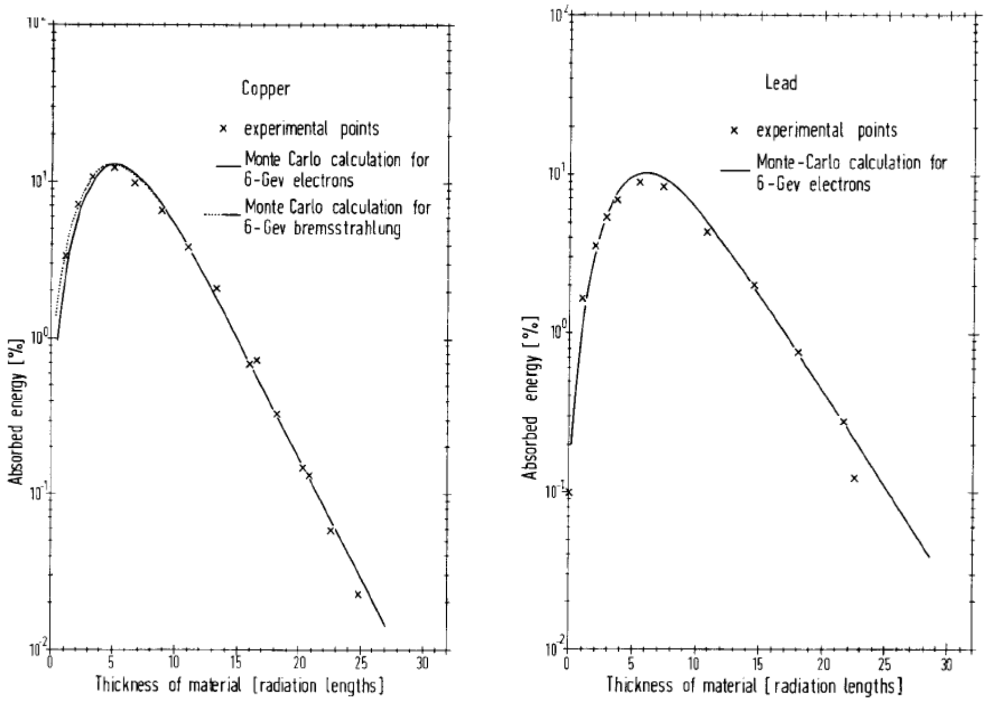

(a) Longitudinal development of the EMC in copper

(b) Longitudinal development of the EMC in lead

Figure 7.3: Longitudinal development of the electromagnetic shower induced by 6.3 GeV electrons in copper and lead [36].

function[1]. A longitudinal energy profile of the EMC is shown in Fig. 7.3 and the basic properties of the EMC are summarized in Table 7.1.

Table 7.1: Approximate EMC quantities ($y = E_0/\epsilon$, where E_0 is the initial energy of the incoming particle) [30].

	Incident electron	Incident photons
Peak of shower, t_{max} $[X_0]$	$1.0(\ln y - 1)$	$1.0(\ln y - 0.5)$
Center of gravity, t_{med} $[X_0]$	$t_{\mathrm{max}} + 1.4$	$t_{\mathrm{max}} + 1.7$
Number of e^+ and e^- at peak	$0.3y(\ln y - 0.37)^{-1/2}$	$0.3y(\ln y - 0.31)^{-1/2}$
Total track length, T $[X_0]$	y	y

The transverse properties of the EMC can be also easily quantified. In the early phase of the cascade, the spread is characterized by both the typical angle for

[1] The gamma function is defined by the relation:

$$\Gamma(z) = \int_0^{\infty} t^{z-1} \mathrm{e}^{-t} \, \mathrm{d}t \, .$$

bremstrahlung emission, $\theta_{\text{brems}} = p_e/m_e$, and multiple scattering of the electron. For the purpose of the energy measurement, the EMC is situated in a cylinder of radius

$$R \approx 2\rho_M\,; \quad \rho_M = 21X_0/\epsilon \approx 7A/Z\,[\text{g cm}^{-2}]\,, \tag{7.4}$$

where ρ_M is called the 'Molière radius' which describes the average lateral deflection of the electrons of the energy ϵ after transversing one radiation length. The Molière radius characterizes the minimal distance of two photons that can be distinguished from each other.

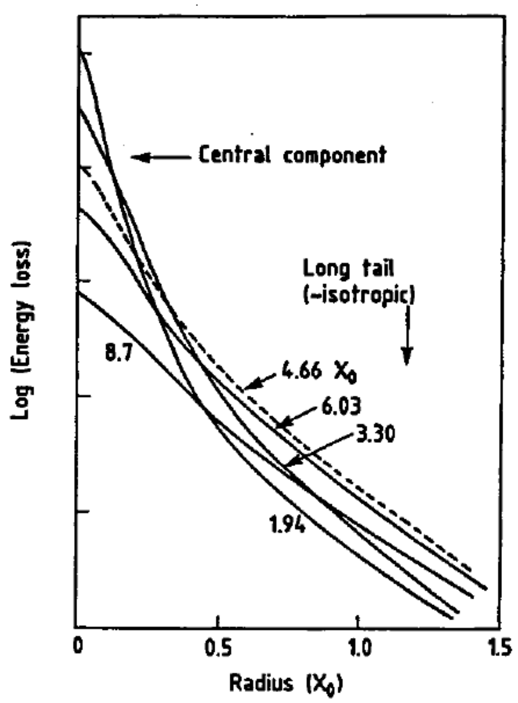

Figure 7.4: Radial profile of the EMC of 1 GeV electrons in aluminium; a pronounced central core, surrounded by 'halo', gradually widens with increasing depth of the shower [30].

7.1.2 Sampling calorimeters

The sampling calorimeters are made of plates of absorber with high density and high proton number Z (such as Fe, Pb or W), between which layers of sensitive medium (scintillators, silicon detectors), that typically have rather low Z, compared to the absorber, are placed. This design allows the sampling (or sandwich) calorimeters to be relatively compact devices. The disadvantage to the sandwich construction is that the resolution worsens, due to the volume of "dead" material in between the detectors.

7.1.3 Fully active calorimeters

If an active material with very large Z is used, we can get completely rid of the inactive absorber layers. Examples of these calorimeters are crystals, like BGO, $PbWO_4$, or lead glass.

7.2 Hadronic calorimetry

The strongly interacting high-energy particles, such as protons, pions, and kaons, produce, in advance to the EMC, a strongly interacting hadronic shower. As opposed to the EMC, the hadronic cascade is not fully analytically described yet [23] but a large amount of empirical data and Monte Carlo simulations is available. A big advantage of the calorimetry is that it is capable of measuring neutral particles. The resolution worsen, however, because of the fluctuations between the electromagnetic and hadronic components of the shower.

Chapter 8

Physics motivation for FoCal

As a next upgrade to ALICE a new forward calorimeter (FoCal) is proposed to be built [29]. This device is designed to measure prompt photons in the pseudorapidity range of $2.5 \sim 3 < \eta < 4.5 \sim 5$ (depending on final design choice). It will cover the full azimuth and will be able to detect photons from a few GeV up to ≈ 100 GeV. Moreover, the FoCal must have good resolution to distinguish the prompt photons from fragmentation photons and to separate photons from the π^0 decay at high momenta. It will also be able to measure jets.

8.1 Nucleon parton distribution at small x

Thanks to the factorization theorem of QCD, we can split the cross section for hadron production in hard-scattering processes of nucleon-nucleon collisions into short-distance and long distance contributions [40, 64]. The leading contribution to the cross-section of a hard process between two partons a and b, from hadrons A and B, can be written as

$$E_h \frac{\mathrm{d}\sigma_{AB\to h(p)}}{\mathrm{d}^3 p_h} = \sum_{abk} \int \mathrm{d}^3 x_2 f_{b|B}(x_2, Q^2) \int \mathrm{d}^3 x_1 f_{a|A}(x_1, Q^2) \int \mathrm{d}z D_{h|k}(z) E_k \frac{\mathrm{d}\hat{\sigma}_{ab\to k}}{\mathrm{d}^3 p_k} \tag{8.1}$$

where $x_1 = p_a/p_A$ ($x_2 = p_b/p_B$) are fraction of the hadrons' momentum carried by the partons a and b, $f(x, Q^2)$ is the parton distribution function (PDF) which means the distribution of the parton momentum fraction in nucleon when resolved at momentum transfer scale Q^2, and the term $E_k\, \mathrm{d}\hat{\sigma}_{ab\to k}/\mathrm{d}^3 p_k$ is the elementary cross-section for the partons a and b to produce parton k with the energy E_k and momentum p_k. The symbol $D_{h|k}(z)$ stands for fragmentation function which defines the probability for the parton k to fragment and produce hadron h, carrying a momentum fraction $z = p_h/p_k$. To obtain the total cross-section, we need to sum over all processes leading to the production of the hadron h, and integrate over all distribution functions and fragmentation functions.

The parton distribution functions are not calculable via perturbative QCD, however they have to be fitted empirically from the data assuming factorization as in equation (8.1) and DGLAP evolution [39, 64]. The NNPDF collaboration has analyzed a large set of experimental data, including deep-inelastic scattering (DIS), Drell-Yan, inclusive jet, and weak vector boson production. These data span a large

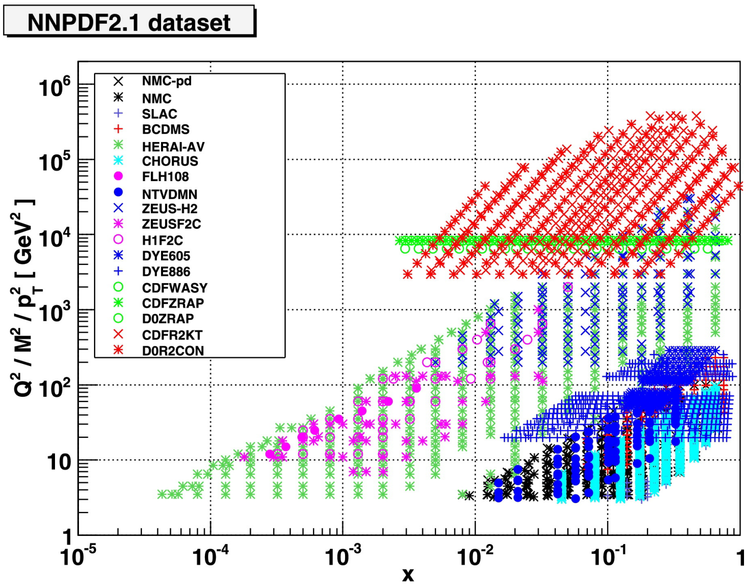

Figure 8.1: The area of x and Q^2 corresponding to the measurements used in the calculation of the NNPDF2.1 PDFs. The analysis includes results from DIS, Drell-Yan, inclusive jet, weak vector boson production, as well as charm production [41].

range of x and Q^2, as illustrated in Fig. 8.1, and were used for determination of NNPDF2.1 [41] PDFs.

While the majority of the p+p physics program measures in the large Q^2, the Pb+Pb program at LHC focuses on the bulk particle production in the p_T range of a few GeV/c where $Q^2(\approx p_T^2) \lesssim 10$ GeV^2 and $x \sim 10^{-3} - 10^{-4}$ where qluons are the dominant partons. In this region, most of the data about PDFs come from the DIS. However, because the gluons do not carry any charge, they cannot be probed directly via the DIS measurements. The PDFs can be calculated indirectly via e.g. momentum sum rules, however this results in that the PDFs have rather large uncertainties.

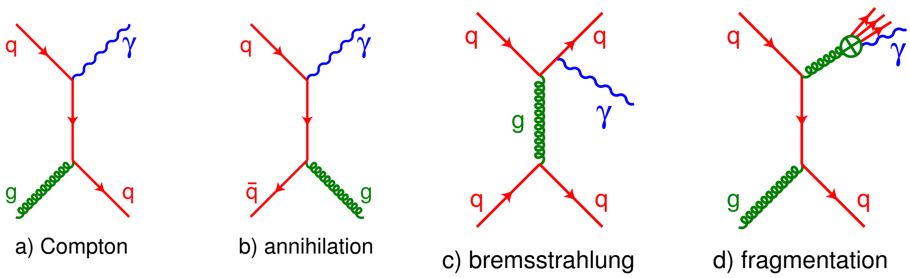

Figure 8.2: Feynman diagrams for photon production. At leading order isolated photons from the a) quark-gluon Compton process, and b) quark-antiquark annihilation process. Non-isolated photons at next-to-leading order from c) bremsstrahlung from a quark, and d) emission during the gluon fragmentation process [29].

Thus, the measurements of the direct photons can constrain the PDFs and strongly lower their uncertainties. The photon production processes at the leading order are shown in Fig. 8.2.

8.2 Nuclear parton distributions and gluon saturation

The parton distribution function of a nucleus with N neutrons and Z protons is not trivially prescribed by a superposition of the PDFs of N neutrons and Z protons [44]. Instead, the nuclear PDFs (nPDF) have to be measured experimentally from nuclei collisions in very similar manner as the nucleon PDFs.

In the region of small x and Q^2, it is expected that the parton density will become so large that non-linear effects due to gluon fusion will arise and undermine the DGLAP predictions [42, 43]. This is called region of 'gluon saturation' or 'color glass condensate' (CGC), and will modify the initial conditions of the nucleus–nucleus collisions The experimentally accessible region of gluon saturation expands significantly with the increased $\sqrt{s}$ of LHC. The kinematic extent with p+A (or d+A) collisions at LHC and RHIC is shown in Figure 8.3.

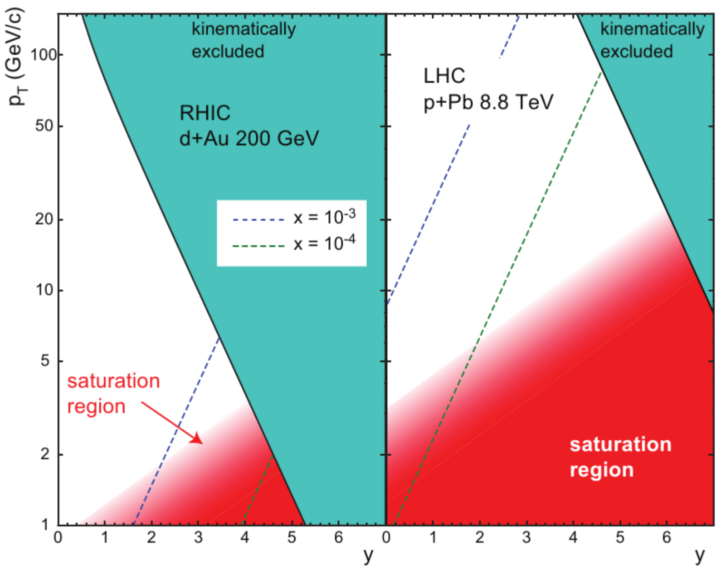

Figure 8.3: Accessible phase space for hadron production as a function of rapidity y and transverse momentum p_T, in collider experiments at RHIC and LHC. The red areas indicate estimates of the region where gluon saturation should be observable ($p_T < Q_s$) [29].

To study the gluon saturation, study of prompt photons as low as possible in p_T is needed. Conclusive evidence will be observed through measurements of a deviation of particle yields from perturbative QCD predictions, using linear evolution.

The nuclear effects on particle productions from nucleus–nucleus collisions are quantified by the nuclear modification factor

$$R_{AB} = \frac{\frac{1}{p_T}\frac{\mathrm{d}N^g_{AB}(b)}{\mathrm{d}p_T}}{\langle N_{\mathrm{coll}}(b)\rangle \frac{1}{p_T}\frac{\mathrm{d}N^g_{\mathrm{pp}}}{\mathrm{d}p_T}} . \tag{8.2}$$

This formula applies for a nucleus of mass number A colliding with a nucleus of mass number B, at the impact parameter b. The term $1/p_T \cdot \mathrm{d}N^g_{AB}(b)/\mathrm{d}p_T$ is the invariant yield of the particle g per event, at the given impact parameter, $1/p_T \cdot \mathrm{d}N^g_{\mathrm{pp}}/\mathrm{d}p_T$ is the invariant yield of the particle g per inelastic p+p collision, and $\langle N_{\mathrm{coll}}(b)\rangle$ is the average number of binary nucleon–nucleon collisions at the given b. With the absence of the nuclear effects the modification factor should be $R_{AB} = 1$.

8.3 The physics case of forward calorimeter at ALICE

Unique physics signals will be obtained from the measurements of direct photons and neutral mesons (π^0, η, etc.) at forward rapidity at the LHC, for all pp, pA and AA collisions. In Table 8.1 the pseudorapidity coverage of the proposed FoCal is compared to other detectors at LHC. It is clear that FoCal outperforms the existing forward detectors in both, maximum reached pseudorapidity and spatial resolution.

Table 8.1: Pseudo-rapidity ranges and granularity of existing forward calorimeters at LHC and the ALICE FoCal proposal [29].

	ATLAS Inner Wheel	CMS EndCap	LHCb ECAL	ALICE FoCal
η range [-]	2.5 – 3.2	1.5 – 3.0	1.8 – 4.3	2.5 – 4.5
granularity [deg]	5.7	0.5	≥ 0.18	≈ 0.016

Figure 8.4 shows that the existing DIS and DY measurements are limited to $x < 10^{-2}$, and measurements at RHIC could extend the kinematic reach up to $x \approx 10^{-4}$, but for very low Q^2 only. The LHC has the potential to significantly extend the reach of the measurements into higher Q^2. The measurements of jets and isolated photons at CMS around mid-rapidity provide additional constrains while the forward measurements, e.g. from LHCb, reach much further towards small x but are limited by relatively low Q^2 ($\approx p_T$). The FoCal extend the available phase space from low to intermediate Q^2 at small x.

In general, the measurements in the forward region probe the PDFs in the small x region. It is possible to measure single hadrons, which however involves a large uncertainty in the measurement due to unavoidable error on the initial state kinematics from the fragmentation process. A fully reconstructed jet measurements would mitigate this problem, these are however restricted to larger Q^2 only, and as such they are not suitable to study the gluon saturation region. The sensitivity of FoCal for prompt photons is shown in Figure 8.5 which shows the cross-sections for three different kinematic cuts simulated in PYTHIA [29]. These predictions display

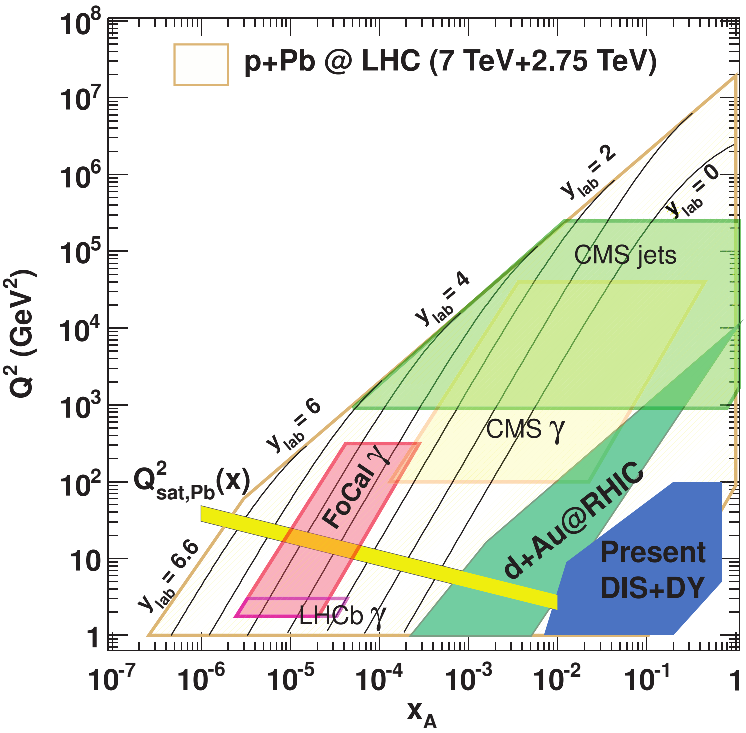

Figure 8.4: Phase space as a function of x and Q^2 for high-energy collisions as estimated from leading-order kinematics. Shown is the kinematic reach for p+A collisions at the LHC and the region studied by DIS and Drell-Yan on nuclei as well as in d+Au collisions at RHIC. Indicated is also the region studied with isolated photons and jets by CMS (currently in p+p), and estimates of the reach of direct photon measurements in LHCb and with the FoCal detector upgrade in ALICE. An estimate of the saturation scale Q^2 as a function of x is shown as the yellow band [29].

clearly that the FoCal will be sensitive to photons at $x < 10^{-5}$ even at rapidity $3.5 < y < 4.5$.

Photons have the advantage that a smaller x can be reached than from the measurements of jets the same rapidity. This can be clearly seen in Figure 8.6 from PYTHIA simulations which shows ranges of x as a function of rapidity for reasonable values of p_T.

In conclusion, direct photons are ideal probe for the low x physics, with a great sensitivity to initial conditions. Moreover, the kinematic conditions at forward rapidities play well for the photon measurements because the irreducible background from neutral hadrons will be much smaller than in the central rapidities.

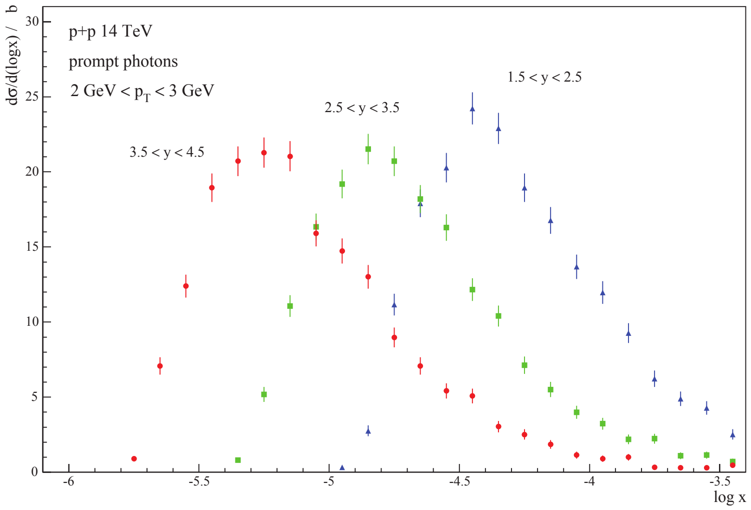

Figure 8.5: Cross-sections of direct photons production as a function of the lower Bjorken-x of the incoming partons (calculated with PYTHIA 8 in p+p at 14 TeV). The photons were constrained to have only $2 < p_T < 3$ GeV/c [29].

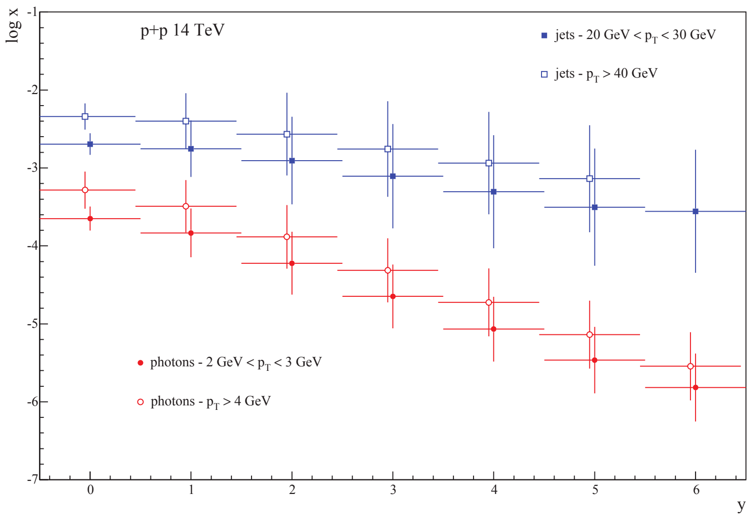

Figure 8.6: Mean values of the smaller Bjorken-x (logarithmic scale) of the incoming partons for the production of jets and direct photons as a function of the rapidity of the final state particle as calculated with PYTHIA 8 in p+p at 14 TeV. The vertical error bars indicate the spread (1σ) of the corresponding x distributions [29].

Chapter 9

Design concept of FoCal

9.1 General design considerations

The main physics objective of the FoCal detector is the measurement of the direct protons at forward rapidities [29]. As the photon detector (electromagnetic calorimeter) it will have to discriminate neutral mesons (e.g. π^0) from the single photons at high energy. This requires relatively very high granularity. Moreover, it should have very good energy resolution and linearity and cover pseudo-rapidities $\eta > 3$.

If these requirements are fulfilled, the detector will also allow to measure neutral mesons (π^0, η, ω, etc.) and to fully reconstruct jets. Furthermore, the high granularity makes measurements in Pb+Pb collisions, where the particle density is expected to be very high, possible.

To meet these requirements, especially the γ/π^0 separation, a sampling type calorimeter design was chosen with tungsten as absorber because of its low Molière radius R_M. The properties of W are:

$$R_M = 9 \text{ mm}$$

and

$$X_0 = 3.5 \text{ mm}$$

(see Chapter 7). The sampling layer thickness will be $\approx X_0$ and the transverse cell size should be in the same order of magnitude as R_M, however for the π^0 identification granularity up to 1 mm proved useful (according to simulations [29]). The high resolution also enhances the capability to recognize multiple tracks. The large number of cells would, however, produce too large volume of data for analysis and unnecessarily increase the cost. The preferable designs are, therefore, with a few high granularity layers combined with layers with moderate cell size.

The acceptance in pseudorapidity depends on the position of the detector: The z-distance from the interaction point and the radial distance from the beam directly influence the pseudorapidity extent $\eta_{\max}$. In Figure 9.1 on the lef hand side, the relation between $\eta_{\max}$ and the z-distance from the IP is shown. The default position of FoCal is set as replacement of the former ALICE sub-detector PMD at $z \approx 3.5$ m. This position allows for $\eta_{\max} = 4.2$ for the inner radius of 10 cm. An alternative scenario at $z = 8$ m was considered which would extend the pseudorapidity reach to ≈ 5. However, an important magnet for the running of ALICE is placed at $z = 8$ m,

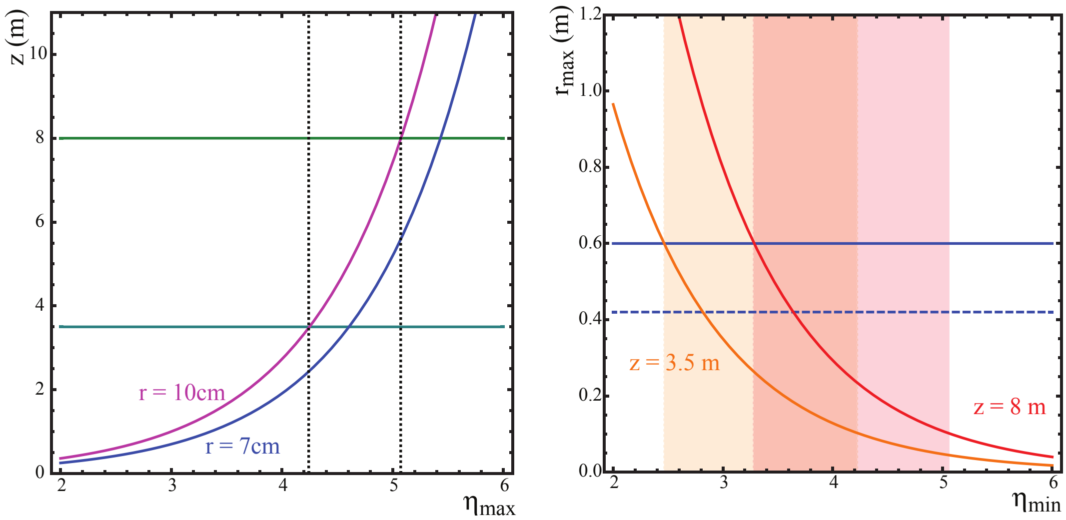

Figure 9.1: Left: z-distance as a function of maximum pseudorapidity η for two minimal radial separations from the beam. Two potential positions in z are indicated as horizontal lines. Right: Outer radius of the detector as a function of the minimum pseudorapidity for two values of z. Two possible radii are also shown. The pink areas indicate the possible η-coverage of the two potential geometries [29].

therefore, more realistically the detector could be positioned at $z \approx 7$ m [49] where $\eta_{\text{max}} = 4.9$ could be reached.

The right hand side of Figure 9.1 shows the dependence of the outer radius r_{max} on the minimum pseudorapidity η_{min}. A detector with the outer radius of $r = 0.6$ m at $z = 3.5$ m would cover up to $\eta_{\text{min}} = 2.5$.

The beam pipe provides another challenge for the measurements at large η. The amount of material that the potentially detected particles have to cross increases dramatically with the decreasing angle θ. Fig. 9.2 illustrates the photon conversion probability P_{conv} for an Al beam pipe of 0.8 wall thickness. The probabilities for the maximum considered η would be $P_{\text{conv}} \approx 0.2$ for $\eta_{\text{max}} = 4.2$, and $P_{\text{conv}} \approx 0.4$ for $\eta_{\text{max}} = 5$. The probabilities may seem high, however the conversions will occur very close to the detector area, therefore this amount of material thickness could be tolerable.

Two major straw man designs are being developed for the sensitive layers: one with silicon detectors and a second one with scintillators. The scintillator design will be discussed in more detail in Chapter 10 because it is one of the main topics of this thesis.

9.2 Silicon detector design

In this concept, FoCal would consist of ≈ 3.5 mm thick ($\approx X_0$) tungsten layers between witch two kinds of sensitive silicon layers are positioned (see Fig. 9.3):

1. low-granularity layers (LGL) of an effective granularity of ≈ 1 cm^2, i.e. of the same order as the Molière radius R_M, and

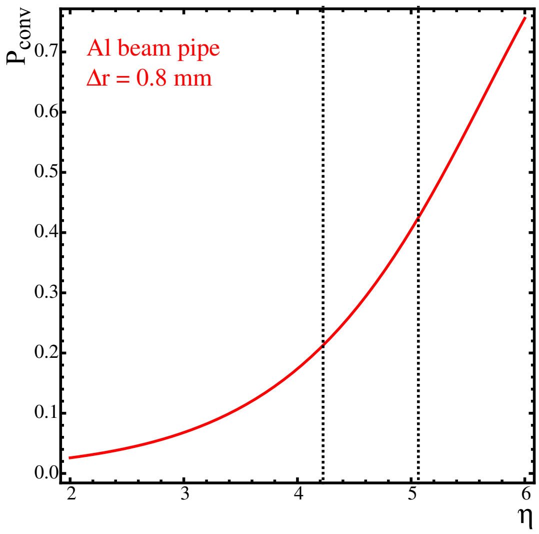

Figure 9.2: Probability for photon conversion in an Al beam pipe with the wall thickness of 0.8 mm as a function of η. Maximum η values for two possible z are indicated with vertical lines [29].

2. high-granularity layers (HGL) with the transverse cell size of ≈ 1 mm^2, i.e. much smaller than R_M.

The preferred technology for the HGLs is monolithic active pixel sensors (MAPS). Because they are based on the CMOS technology, they are moderately cheap. This technology can provide binary signals from pixel sizes down to 20×20 μm^2. This signal will be processed on-chip to pixel count in 1×1 mm^2 macro-pixels.

The downside to the MAPS technology is that they are intrinsically slow. Firstly, that means that they will not provide a trigger signal. Secondly, while the $5 - 10$ μs integration time should be low enough to discriminate different events in Pb+Pb collisions, pile-up will occur in the p+p collisions so they will have to be disentangled by the time measurement of the LGLs.

In this design, the LGLs use conventional silicon pad sensors. The analog signals from the same transverse location will most likely be summed along the different layers and digitalized with available electronics.

The number of HGLs is still under investigation. Their placement near the shower maximum would be most beneficial, due to the larger height of the signal. The position of the shower maximum is, however, energy dependent, and moreover, it fluctuates from event to event. Furthermore, the track separation capabilities may be more optimal at shorter distances. Therefore, this is not the single best placement of the HGLs.

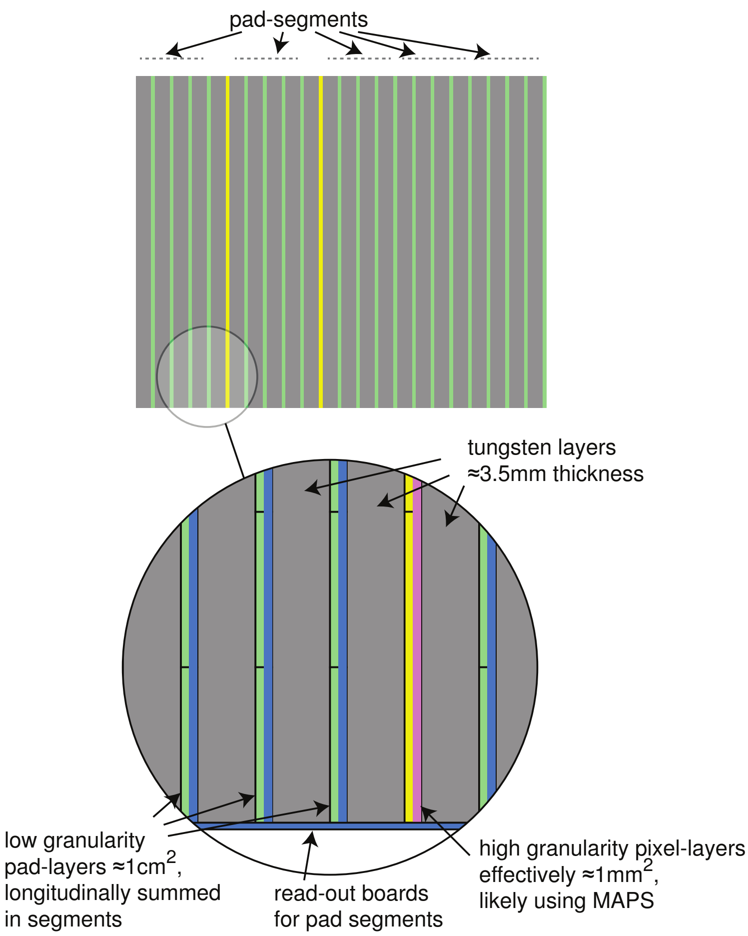

Figure 9.3: Schematic view of the longitudinal structure of the silicon detector concept of the FoCal [29].

Chapter 10

Scintillator design concept of FoCal

A new design concept of FoCal is being developed by the Czech Technical University in Prague. We propose that a hybrid calorimeter is used, with ≈ 3.5 mm tungsten layers as an absorber (the same as in Section 9.2). However, instead of the silicon detectors, scintillators are used as the sensitive medium.

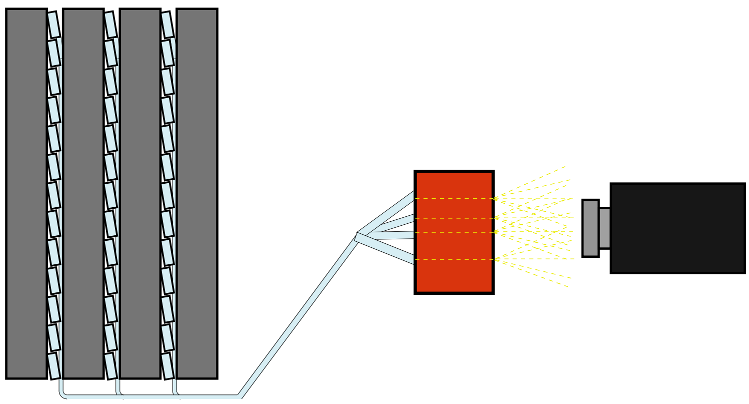

Figure 10.1: Illustration of the scintillator design concept of FoCal. The light is read out from the scintillators via optical fibers that lead into an image intensifier which amplifies the light signal by a factor of $\sim 10^7$. The image intensifier is being observed by a very fast 5 MPx digital camera.

Our design concept is illustrated in Fig. 10.1: The traversing particle creates an electromagnetic cascade in the detector volume. Consequently, the particles from the EMC, crossing the scintillator area, induce light production which is read out via optical fibers. The light is than guided into a very fast image intensifier, capable of amplification up to $\approx 10^7$. The image from the image intensifier is than taken by a very fast 5 MPx camera.

The scintillators have several advantages, compared to the silicon detector concept:

- Because the particle multiplicities are generally very high at large pseudorapidities (small x), the detector must be very resilient to the radiation induced degradation. The scintillators are very radiation-hard detectors, therefore, they are an ideal candidate for the sensitive part of the calorimeter.

- The scintillators do not need cooling and electric power supply which would be absolutely necessary for the silicon detectors and would increase the dead area of the detector.

- This design concept is significantly cheaper than the silicon detector alternative.

10.1 Scintillation pads

The detector pads will most probably consist of plastic scintillators, because of their excellent radiation hardness, good material qualities and relatively low cost. However, the scintillation material has not been chosen yet. The most probable candidate is 3HF [59, 60] because of its radiation hardness.

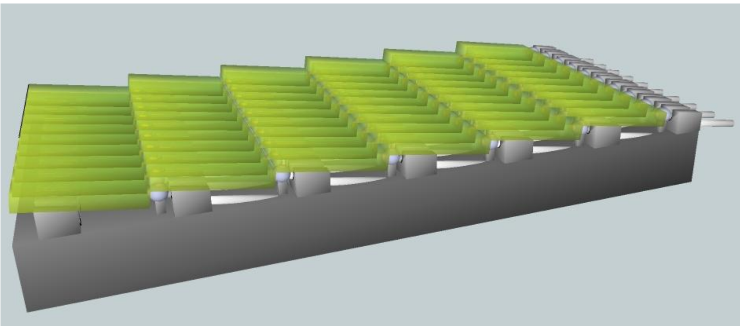

(a)

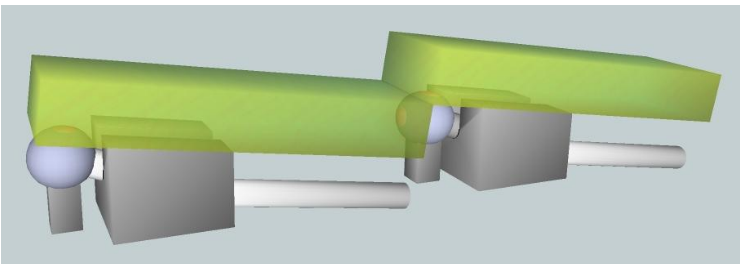

(b)

Figure 10.2: (a): View of one layer of scintillators, mounted to a tungsten absorber plate. (b): Detail of scintillator pad mounting, together with the optical fiber readout. Optical readout via a spherical lens, attached to one end of the optical fiber, is drawn.

The pads will be mounted on the tungsten layer under an angle so that dead area in the detector is avoided (see Fig. 10.2). The optical information will be read out by optical fibers, attached to a side of the pads. The pads will be glued to a support structure that also holds the optical fibers which than fill the space between the scintillators and tungsten.

The size of the pads is currently under investigation, however their maximum size is in the order of R_M. More simulations will be needed to be able to make a final decision.

10.2 Scintillator readout

The optical readout of the pads is currently under investigation. There are three possibilities available:

1. The fibers are glued directly to the scintillation pads via optical varnish. This is the simplest solution, however some photons will be lost because of the low angular acceptance of the optical fibers.

2. A spherical lens (a microscopic transparent sphere) is glued to the end of the optical fiber (as in Fig. 10.2(b)), so that the interface between the pad, the air, and the sphere bends the photons' trajectories into the optical fiber (see Figure 10.3). Some information is lost, however, by reflection on the surface of the scintillator and the sphere.

3. A wavelength shifter (WLS) is either glued to the pad surface or cast into the scintillator volume. A wavelength shifter [23, 67] is a material that absorbs photons in a certain frequency window and emits it back into 4π geometry with a higher wavelength (The WLS "feels" the light with its surface). A disadvantage of this solution is that the properties of the WLS worsen in high-radiation environment. Thus, the radiation hardness of the whole detector drops significantly with the introduction of the WLS.

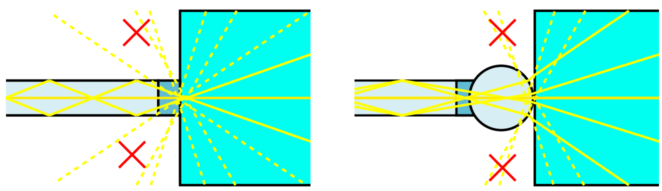

Figure 10.3: An illustration of geometrical acceptance of an optical fiber without (on the left) and with (on the right) a spherical lens.

10.3 Camera

A commercially available high-speed camera system 'FastCamera13' by FastVision company was chosen [68,69]. This camera is based on CMOS imager with a trigger-able global electronic shutter [70]. It is equipped with an integrated high-speed

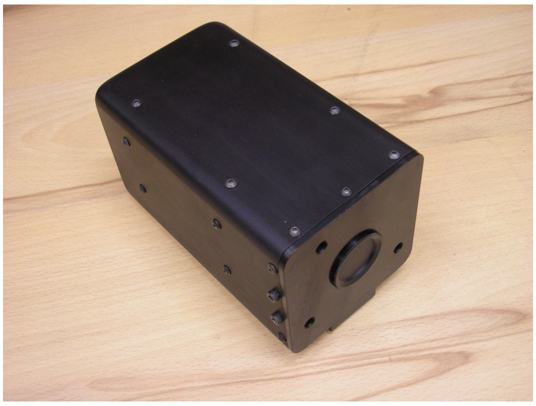

Figure 10.4: Photograph of FastCamera13 without an objective.

FPGA which enables in-camera high-speed processing. The maximum resolution is 1280×1024 pixels with 500 frame rate per second, however the frame rate can be increased up to 500000 fps with only one row read out (1×1280). A photograph of the camera is shown in Figure 10.4.

10.4 Simulations of the optical readout

Monte Carlo simulations of the optical readout were made by Bc. Roman Lavička [50, 61] in the optics simulation program 'SLitrani' [62, 63], based on ROOT.

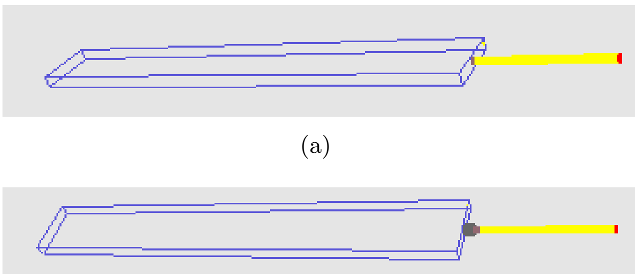

(a)

(b)

Figure 10.5: Geometry used in readout simulations. Photons are emitted in a scintillator with dimensions $5.2 \times 1 \times 40$ mm^3 and are read out in (a) an optical fiber glued to the scintillator, and (b) an optical fiber with a spherical lens (grey sphere) glued to its end. The layer of glue is simulated as optical varnish. The photons that traverse the red area are counted as detected.

The geometries, used in the simulations, are shown in Figure 10.5. First, a scintillation material of $5.2 \times 1 \times 40$ mm^3 is read out by an optical fiber glued to the scintillator surface via optical varnish, and second, a spherical lens, glued to an optical fiber, is used for readout. 10000 photons were emitted isotropically in various points inside the scintillator. Results in 1 mm (Fig. 10.6) and in 3 mm (Fig.

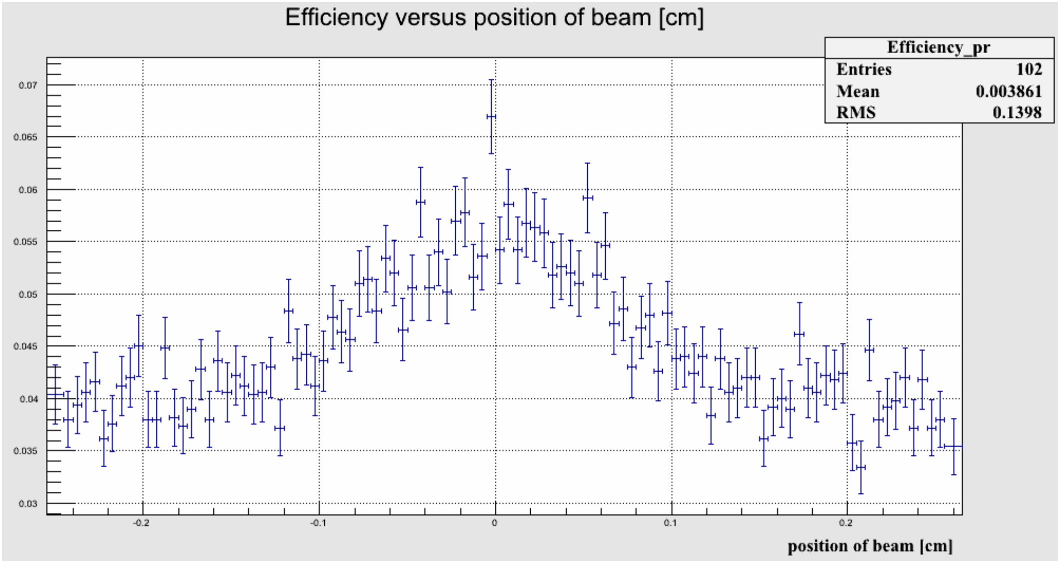

(a) Readout via glued optical fiber.

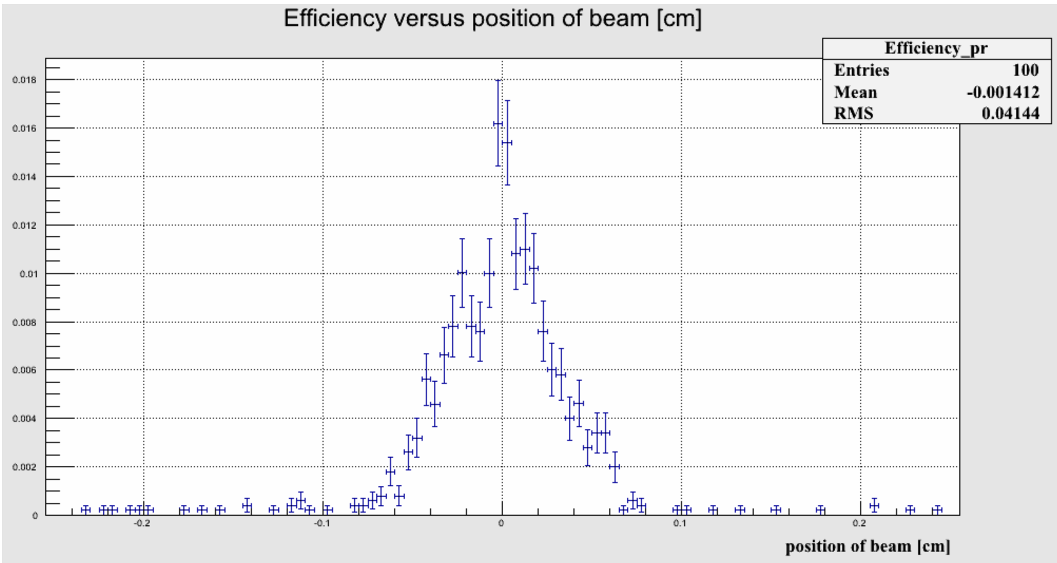

(b) Readout via spherical lens.

Figure 10.6: A simulation of optical readout efficiency with 10000 photon emitted isotropically in various positions in 1 mm distance from the right side of the scintillator.

10.7) from the side of the scintillator with the attached readout, are shown in plots of the efficiency vs. the position of the emitting point.

The results show clearly that the fiber, glued directly to the scintillator pad, has larger geometrical acceptance. Moreover, the efficiency of readout of this variant is better by an order of magnitude. Thus, the option with the spherical lens seem significantly worse, in this simulations. This huge difference is probably caused by

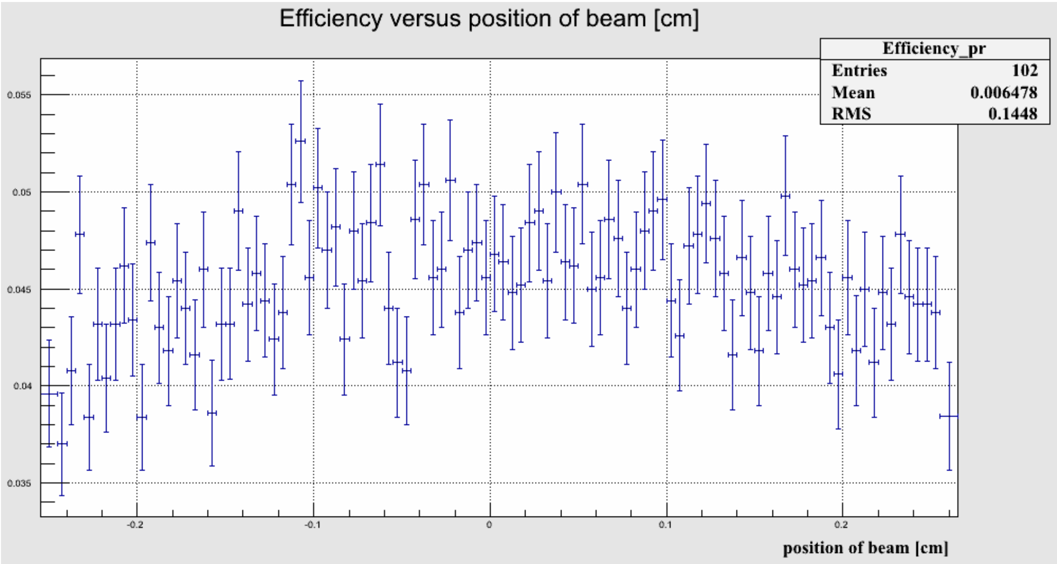

(a) Readout via glued optical fiber.

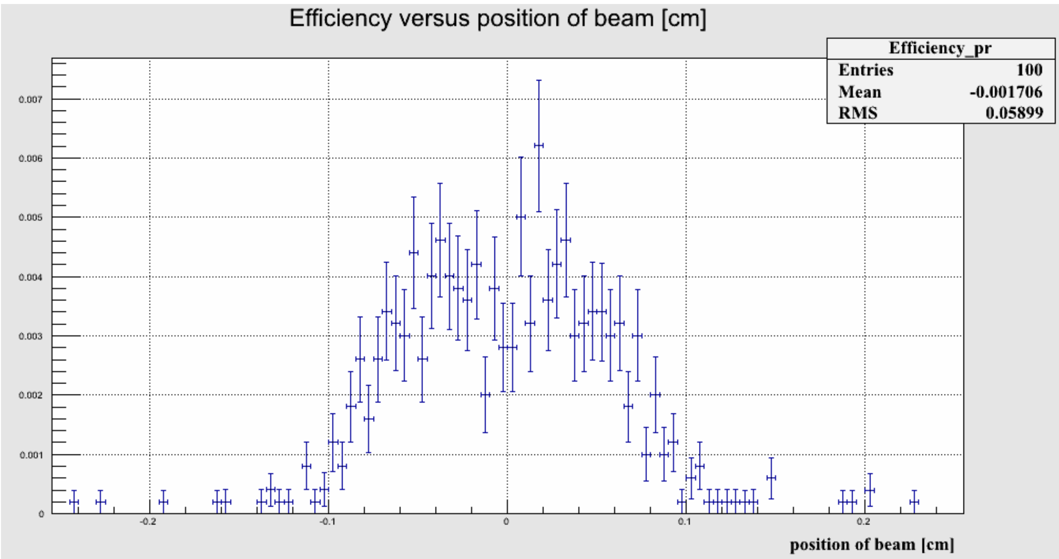

(b) Readout via spherical lens.

Figure 10.7: A simulation of optical readout efficiency with 10000 photon emitted isotropically in various positions in 3 mm distance from the right side of the scintillator.

reflection on the surface of the spherical lens. This could be overcome by anti-reflexive coating of both, the scintillator and the lens which is, however, rather technologically difficult.

The slices, shown in Figures 10.6 and 10.7, were made in several distances from the readout. The width of the signal in half of its maximum (FWHM) was plotted as a function of the distance in Figure 10.8.

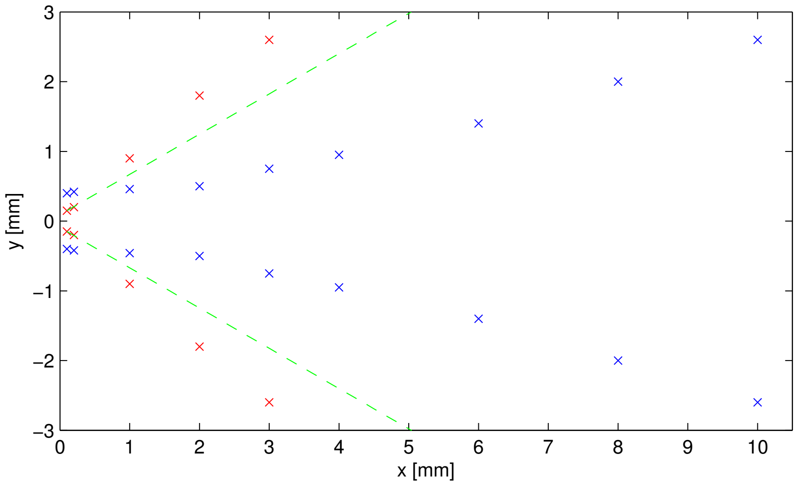

Figure 10.8: Plot of the geometrical acceptance of the optical readout, according to simulations. From the same simulations as shown in Figures 10.6 and 10.7, the width in a half of the maximum of the signal (FWHM) was plotted (y) as a function of distance from the side with the attached readout (x). The red crosses show the acceptance of the readout variant with the optical fiber glued to the scintillator and the red ones are from the option with the spherical lens. The green dashed lines show the 30° acceptance (the total reflection in the fiber occurs at the 30° angle). The readout is attached at the point [0, 0].

The optical fiber without the spherical lens first copies the 30 degrees acceptance, which is the angle of total reflexion on the fiber's surface, and than the signal even widens a little. The acceptance of the spherical lens is a little wider at the beginning but than does not broaden as much and shortly, even the 30° acceptance is a lot wider.

Overall, the simulations show that the spherical lens reads out a lot less space than the fiber alone. Moreover, the height of the signal favors the directly glued fiber too. Therefore, the spherical lens readout, in the current geometry, does not seem like a plausible option.

The problem with these simulations is the behavior of the light on the surfaces of the used materials. It is hard to define precisely the properties of the surfaces because many factors may play an important role on the traversing photons. Thus, the real efficiency of the readout has to be measured empirically (see Chapter 11).

Chapter 11

Probing station for scintillator readout

11.1 Overview

In the optical readout, there are many factors that can all significantly influence the readout efficiency e.g. the size of the scintillation pads, and surface treatment of them (like cutting and polishing). Because lots different samples with slightly changed properties have to be tested, a probing station of the readout had to be made.

The layout is shown in Figure 11.1. The main principle of the probing station is simple: The sample of the scintillator pad is placed on a table with a micrometer step under which a radiation source with a collimator is positioned. Like this, we can introduce particles precisely to a wanted location and measure the readout capabilities of the tested sample.

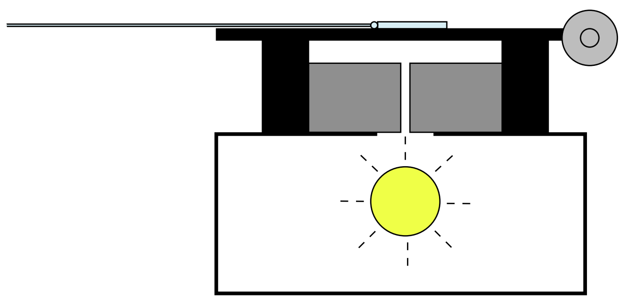

Figure 11.1: Layout of the probing station for the optical readout.

The main requirements for the probing station were to be as safe as possible, easy of use and rigorous in its measurements.

As the source of radiation, an X-ray source was chosen as the best option. It is coupled with a collimator, made of lead 2 cm thick at its thinest part with a 1 mm wide collimation hole. A micrometric table MLC–2 [71] by the LANG company is being used. It employs a very precise stepper motor with 1 μm step that can be operated remotely via joystick or from computer which is particularly useful because the table is placed inside the dark chamber. The probing station ready to use only without a sample is shown in Figure 11.2.

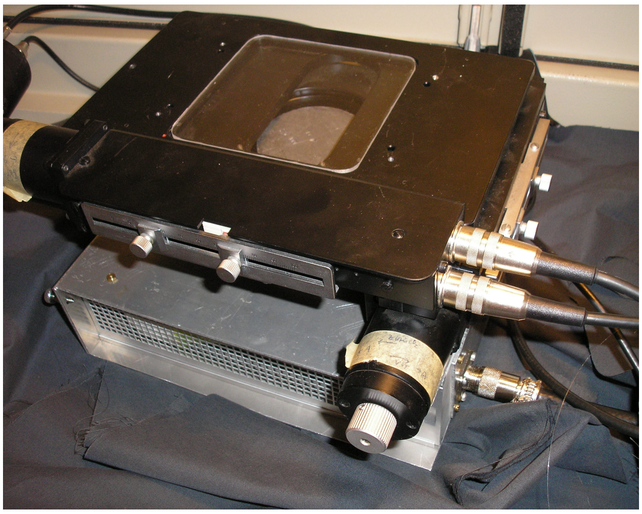

Figure 11.2: Photograph of the assembled probing station inside the dark chamber. The metal box at the bottom is the X-ray source, and the micrometric table (black) is placed on top of it. The collimator can be seen through the transparent plastic window in the table. The cable leading to the X-ray source is a high-voltage (up to 100 kV) power supply and the two cables connected to the micrometric table are its remote control.

In advance to the X-ray source, an alpha source can be used. This setup has the advantage that the collimator can be much thinner, therefore the particle multiplicity is not lowered that much by the geometry. A 1 mm thick plastic plate with a 0.5 mm hole is used as a collimator. The activity of the alpha source, however, has to be fairly high because of the size of the collimation window. A photograph of the alpha source with the collimator is shown in Figure 11.3.

Figure 11.3: A photograph of an alpha source with a plastic collimator.

A 100 kV high-voltage source Technix SR-300 [72] serves as a power supply for the X-ray source and two Bertan 225 series 5 kV sources [73] supply the photomultipliers. All of them are mounted in a rack together with the micrometric table control. A photograph of the rack is shown in Fig. 11.4

Figure 11.4: Photograph of the power sources and of the micrometric table control mounted in the rack. There are from the top to bottom: The micrometric table control, Technix SR-300 100 kV power source, and two Bertan 225 series 5 kV sources.

The readout from the samples is done via two photomultipliers that are coupled with two oscilloscopes which are capable of producing a TTL signal when the trigger is activated. This signal is than counted by a counter controlled from a computer.

The whole measurement is fully automatized and controlled from a single computer. The operator simply defines the area he wants to be scanned, the step length, and the counting time in each step. The probing station than scans in a grid with the defined borders with the step length as the distance between the grid points. For example, the operator submits a 5 mm $\times$ 6 mm area to be scanned with a 0.5 mm distance from each measurement point and in each point he or she wants to count the signals for 60 seconds.

Next, we describe the properties of the used components.

11.2 Dark chamber

The chamber where silicon drift detector for the Ceres experiment were tested. However, some changes had to be made, namely the light leaks had to be sealed. The reworked, sealed, dark chamber is shown in Figure 11.5.

The chamber is positioned on a table with a hole through it where the drift detectors were mounted. This is good because the cables can go through this hole now, however the rest of the hole had to be sealed. Firstly, a carton covered with an aluminum foil was pierced so that the cables could be put through. The carton was than put over the hole and the rest of it was covered with a metal plate.

Figure 11.5: Photograph of the dark chamber with a curtain installed over the front door.

The remaining leakages were sealed with putty, black duct tape and aluminum foil. Moreover, inside the chamber, the whole experiment is covered with dark fabrics, and also a curtain was attached to the front door from the outside.

11.3 X-ray source

The X-rays were chosen for the radiation source for several reasons: They are easily shielded, high multiplicities of the photons can be achieved, and the X-ray source is relatively cheap to build.

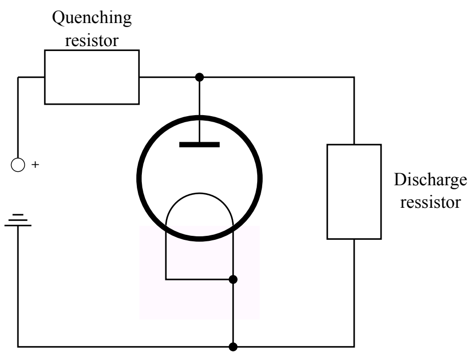

Figure 11.6: Left: Diagram of the X-ray source implementation. Right: Photograph of the DY 87 vacuum tube.

DY 87 vacuum tube diode [74, 75] is used as our X-ray source. It is connected in reverse direction with the input voltage of 25 – 45 kV. After the tension of ≈ 25 kV is reached the tube starts emitting X-Rays, but the optimal values are ~ 35 – 40 kV. The diagram of the source is very simple (see Fig. 11.6): In addition to the vacuum tube diode connected in reverse direction, a 3 MΩ quenching resistor is added so that sudden sparks in the tube are avoided. Moreover originally, a 200 MΩ discharging resistor was connected in parallel as a safety measure because the tube can discharge through it when the power is off. The first discharging resistor was removed, however, due to its instability but it will be replaced with a new one in the future.

A lot of effort was put into the electrical safety measures of the source. All the parts of the X-ray source under electric tension are covered in a thick insulation plastic and placed inside 2 mm thick polypropylene (PP) tubes. The joints of the tubes are lubricated with silicone to prevent the appearance of the sparks on the surface. The vacuum tube is embedded in insulation plastic inside a PP tube. The source is energized by a high-voltage connector with the distance of ≈ 15 cm between the electrodes. The connector is also lubricated with the silicone. Moreover, the whole device is put inside a grounded metal box.

As for the radiation protection: The polypropylene tube with the DY 87 is placed inside a lead tube of ≈ 1.5 cm minimum thickness with only a small hole pierced through it where the collimator is placed. Moreover, the sides are covered from the inside with 1 mm thick lead plates conductively connected to the electric grounding. The photograph of the assembled X-ray source is in Figure 11.7.

11.4 Measurements of the X-ray source properties

After the X-ray source was built, its properties had to be tested: namely the energetic spectrum and geometrical properties of the emitted photons after the collimation.

11.4.1 Spectral measurement

The spectra were measured via a hyper-pure germanium (HPGe) nitrogen cooled spectrometer by Ortec company (a photograph shown in Fig. 11.8). The signal was analyzed in a multichannel counter and than processed in a computer, using ROOT.

Because the spectrum depends very much on the input voltage in the X-ray source, the spectra were measured for several voltages, ranging from 32.5 to 41.5 kV. Firstly, the spectra were normalized, according to the time of the measurement. This was done by integrating the very energetic (> 80 keV) part of the spectra and than the number of counts were multiplied by the ratio between the 37 kV spectrum and the currently processed one. After this, the background was subtracted via a similar process (the background was normalized on the 37 kV, and than subtracted). The spectra are shown in Figure 11.9.

The shape of the spectra stays very similar for all the voltages. The highest multiplicity is measured in at the lowest energies, than it drops in the middle, to be superseded by a peak in the highest kinematically allowed energies. The spectra are ended by a steep edge that quickly goes to zero. The particle multiplicities rise

(a) (b)

Figure 11.7: (a): Photograph of the opened X-ray source. The DY 87 tube is situated inside the lead cylinder in the middle. All of the components, that are under tension, are inside the PP tubes and also embedded in plastic insulation. The orange parts on the sides are 1 mm thick lead plates. (b): Photograph of the assembled X-ray source, equipped with the lead collimator. The high voltage connector is situated on the side. Around the collimator the flange, where the micrometric table is mounted, can be seen.

Figure 11.8: Photograph of the HPGe spectrometer, used in the spectral measurements of the X-ray source.

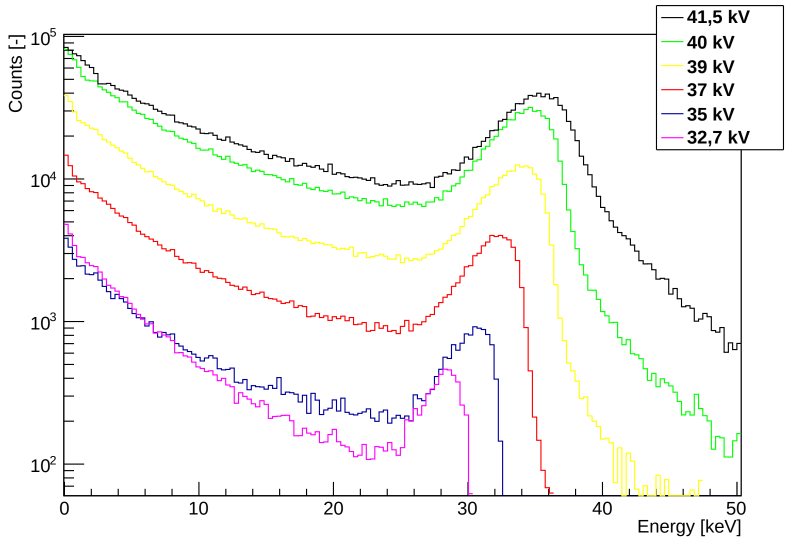

Figure 11.9: X-ray spectra with various voltages on the X-ray source. The logarithmic scale is used on the counts axis.

rapidly with the increasing input voltage (note the logarithmic scale) and between 35 and 40 kV the rise is approximately exponential.

11.4.2 Geometrical properties of the emitted X-rays

Because the properties of the X-ray photons emitted in the DY 87 tube are not very well documented, geometrical properties of our X-ray source had to be measured experimentally. It was also crucial to optimize the tube's position so that the highest possible multiplicity of the emitted photons is achieved. For this purpose, the pixel detector, developed at CERN, Medipix3 [76, 77] was used.

The Medipix3 is a multipurpose pixel detector based on the CMOS technology. Its 14×14 mm^2 chip disposes 256×256 pixels of 0.055 mm size, each. It is powered by a low voltage power source and the data are read out directly via a computer. The infrastructure, used by the Medipix is shown in Figure 11.10.

Measurement with different input voltages on the X-ray source:

After the vacuum tube's position was adjusted to the ideal position with respect to the collimator and fixed there, we measured the X-ray yields with different input voltages on the X-ray source. From 35 kV we went by 1 kV up to 40 kV. Afterwards, the measurement was analyzed via ROOT. The results are plotted in Figure 11.11.

If we look at the results, the area, where the X-rays are emitted, does not make a circle shape, even though the collimator window is almost perfectly round. This is caused by the relative shift of the source from the collimator because the photons traverse the hole at an angle. However, with the rising voltage, another oval shaped spot appears in the detector and has increasing count number. At 40 kV it is even stronger than the original area.

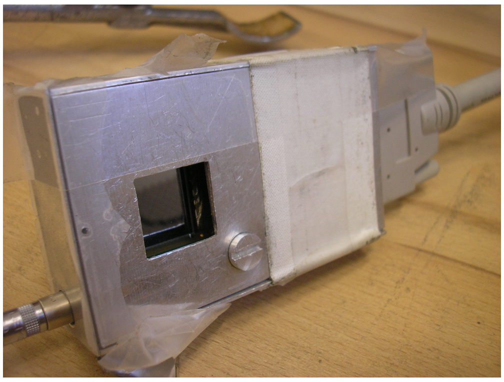

(a)

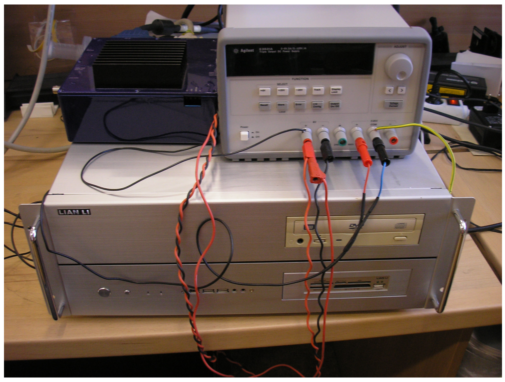

(b)

Figure 11.10: (a): Photograph of the Medipix3 detector. The detector chip can be seen in the window of the detector's aluminum shell. The connector in the bottom left corner serves as a power supply and the wire connected to the right hand side is the readout of the detector. (b): Photograph of the Medipix infrastructure. The blue box on the left is control and readout of the detector and the gray box on the right is the power supply of the detector. Both of them stand on the computer, connected to the Medipix control box.

From this measurement, we conclude that the X-rays are not emitted from the whole area of the cathode, but rather point-like hot spots are created. Moreover, longer measurements show that the count rate is not stable with time. Therefore, when the scintillation pads are tested, another detector for normalization will have to be present.

Divergence measurement:

The Medipix was fixed in six different distances above the collimator, in this measurement. The detector output, analyzed in ROOT, is shown in Fig. 11.12. The voltage on the X-ray source was set to 37 kV.

In addition to the spot with the largest count rates, created by the photons that fly directly from the source, there are several weaker areas that are caused by the reflected photons from the surface of the collimator. The multiplicities in these spots are, however, a lot smaller than in the original area. Lets call the area with the not reflected photons the main spot. The reflected photons can be avoided by placing right underneath the sample another lead plate with a tiny hole pierced through it.

From the histograms, shown in Figure 11.12, slices in both, x and y directions, were made where the main spot is widest. An example of the slices in 2 cm distance from the collimator is shown in Fig. 11.13. This position was chosen because when the whole probing station is assembled, the tested scintillator pads are positioned in 2 cm distance above the collimator.

In the main spot, the plots are relatively flat with very steep, almost vertical edges. Therefore, the width of the spot is very well defined and can be deduced from the measurement of the width in half of the maximum (FWHM). The width

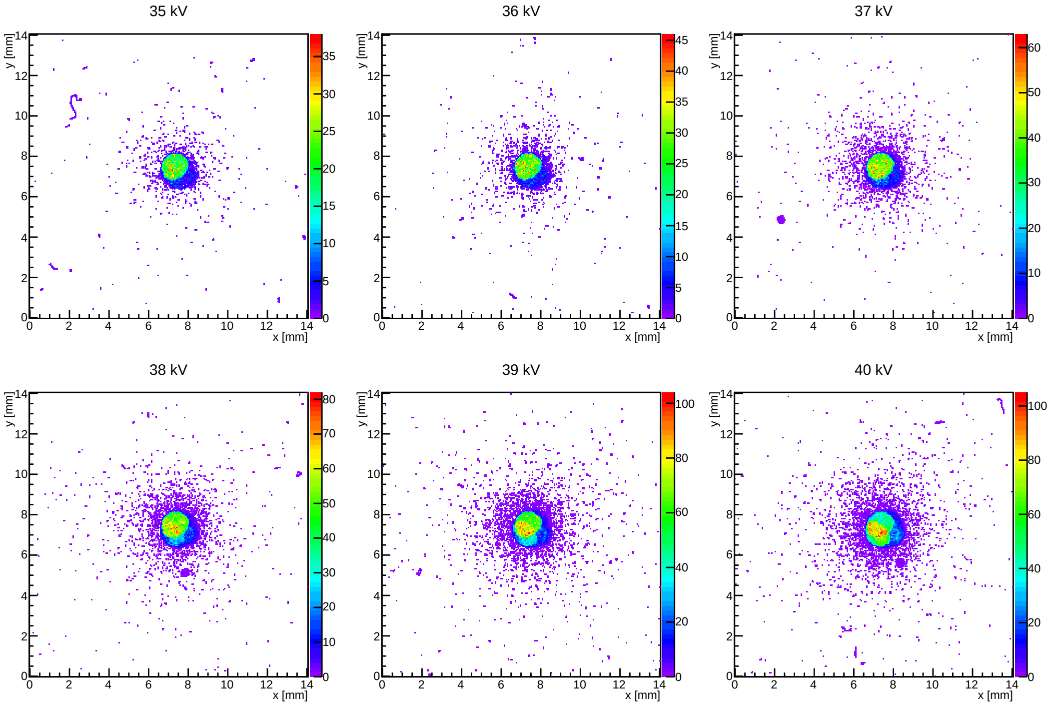

Figure 11.11: Positional measurement of the X-ray source with collimator made with the Medipix detector, positioned directly on the collimator. Measurements were made with 6 different input voltages on the X-ray source, ranging from 35 kV to 40 kV.

of the main spot is plotted versus the distance of the collimator in Figure 11.14 in x direction and in Figure 11.15 in y direction.

The divergence angle can be easily calculated from the fit, to be $(6.0 \pm 0.6)^{\circ}$.

11.5 Photomultipliers

For the readout testing, several photomultipliers were tested. As the best option, two long photomultipliers with 2.2 kV input voltage were chosen because of their relatively good signal to noise ratio.

11.6 Oscilloscopes

Every photomultiplier is connected to an oscilloscope via a coaxial BNC cable. Two oscilloscopes are used: Tektronix DPO 4054 (shown in Fig. 11.17(a)) [78, 79], and RIGOL DS 4014 (shown in Fig. 11.17(b)) [80]. Both oscilloscopes have inputs for 4 channels, both have a USB and ethernet connectors, and both are capable of production of the TTL signal when the trigger is activated. The TTL signals are transmitted via coaxial BNC cabels.

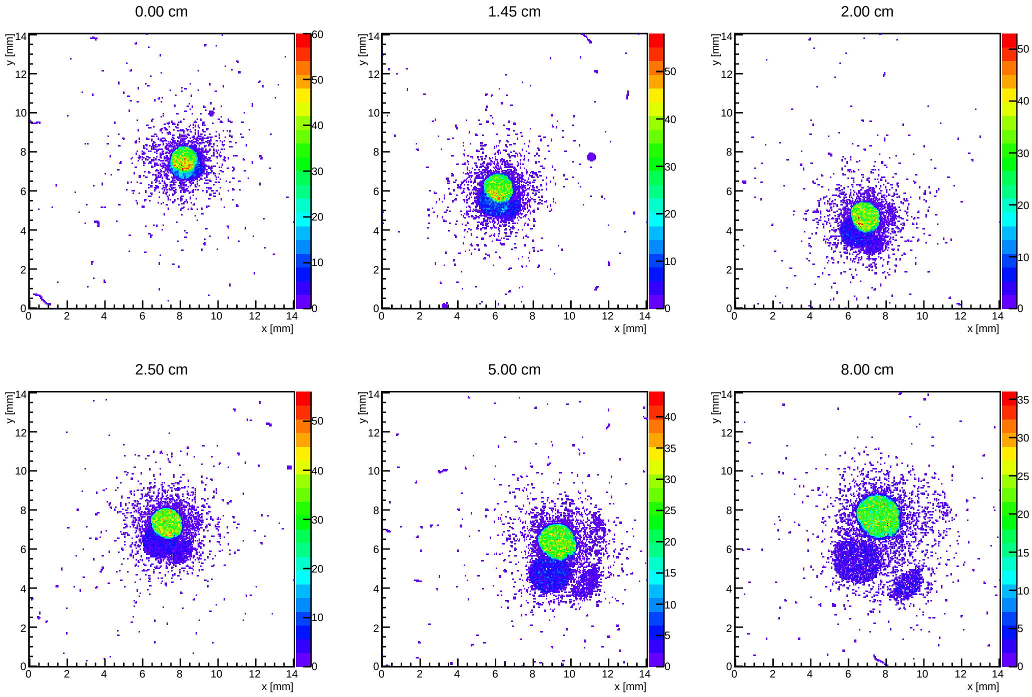

Figure 11.12: The divergence measurement of the X-ray source plus collimator: The Medipix detector was placed in several positions over the collimator. The Medipix output is shown in six distances. The voltage on the X-ray source was set to 37 kV during this measurement.

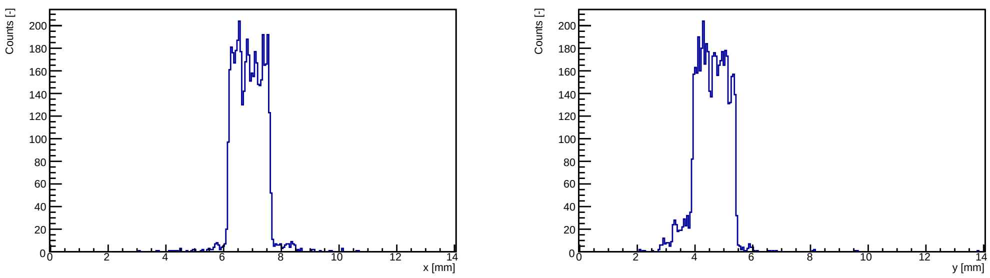

Figure 11.13: Slice of the histogram in x (left) and y (right) direction, measured in 2 cm distance.

11.7 Counter and control

For the automation of the measurement, modules from the National Instruments company were used. This allowed to connect the measurement equipment in such way that, ultimately, it can be fully automatized and controlled from a single computer.

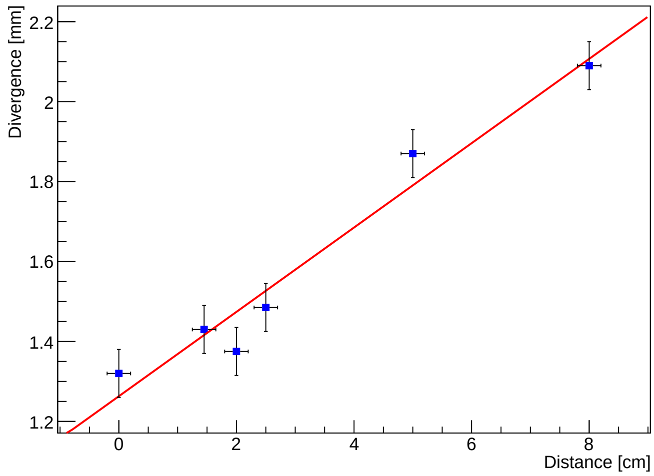

Figure 11.14: Plot of the width of the main spot vs. the distance from the collimator in x direction.

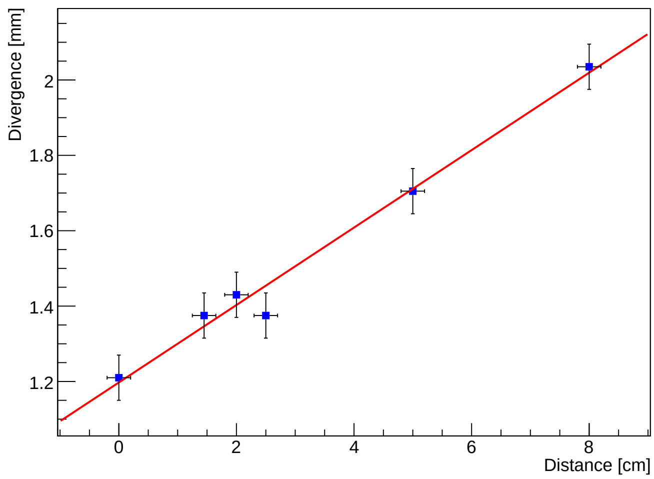

Figure 11.15: Plot of the width of the main spot vs. the distance from the collimator in y direction.

11.7.1 National Instruments modules

All the modules are mounted in a chassis with the name code NI PXIe-1078 [81], and are connected to the PC via PCIe–PXIe card that is interfaced to the PXI interface card named NI PXIe-8360 [82]. A photograph of the NI modules in the chassis is in Fig. 11.18.

For the control of the micrometric table, the RS232 interface module NI PXI-8432/2 [83] is used. In Figure 11.18 it is the rightmost card.

Figure 11.16: Photograph of the photomultiplier used for the readout testing.

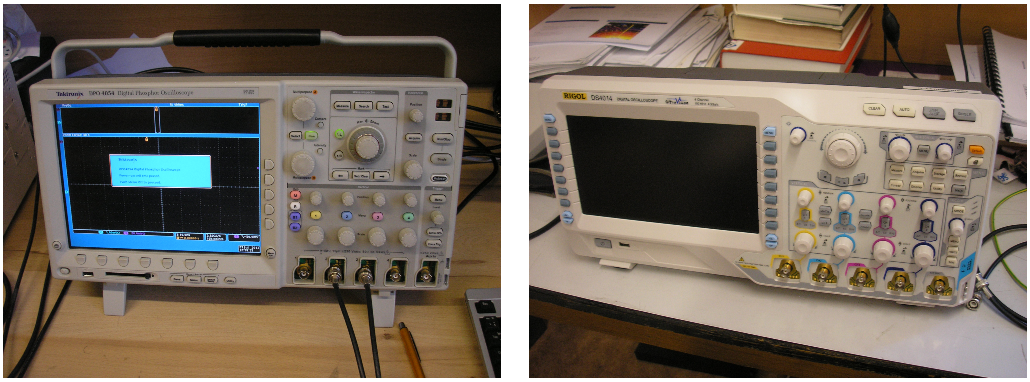

(a) Tektronix DPO 4054 (b) RIGOL DS 4014

Figure 11.17: Photographs of the two oscilloscopes used for the readout testing.

11.7.2 Data Acquisition module

The multipurpose Data Acquisition module (DAQ) NI PXIe-6341 [84,85] is currently used for its counters. The module can, however, serve multiple purposes. It provides 16 analog inputs with range of ±10 V that can measure with 500 kS/s, two ± 10 V analog outputs, and 24 digital input/output lines. In addition to that, the module 4 digital counters with internal clock the with maximum frequency of 100 MHz, however external clock can be used.

The measured or controlled devices are interfaced to the so called connector block. In Figure 11.19, we show an opened connector block with the connected coaxial cables that lead from the oscilloscopes. The coaxial cables are connected to the pins with counters.

11.7.3 Programming in LabVIEW

LabVIEW [86] is a programming and simulation software, developed by the National Instruments company. It provides tools to control the instruments directly or via various set of supported ports, such as GPIB or RS232. Moreover creating of the user interfaces is fairly easy and encouraged by the LabVIEW.

The programs in LabVIEW are called virtual instruments (or VIs) because the

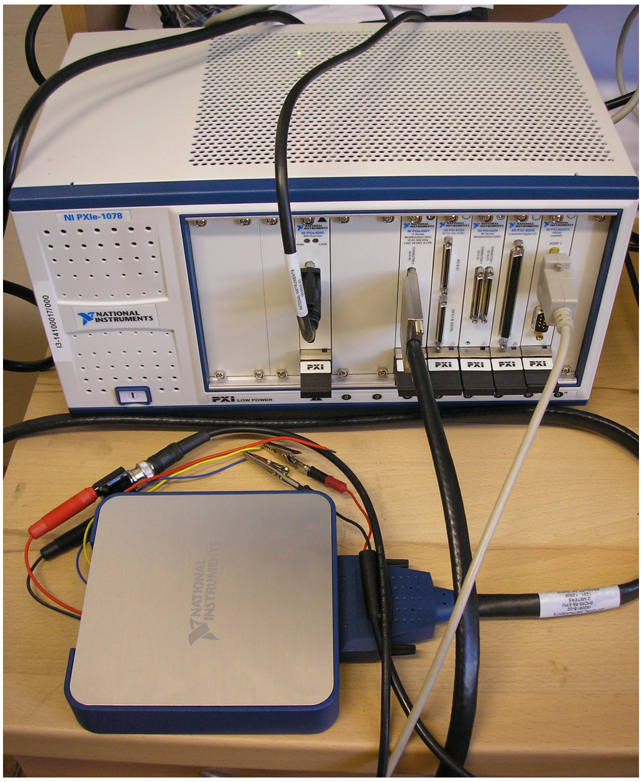

Figure 11.18: Photograph of the National Instruments modules mounted in the NI PXIe-1078 chassis. The first module form the left is the computer interface card NI PXI-8360. The second one is the multipurpose Data Acquisition module (DAQ) NI PXIe-6341 which is currently used as the counter. Finally, the card on the right with the connected is a two SR232 serial port interface NI PXI-8432/2 which currently controls the micrometric table. The blue box in the bottom is a connector block for the NI PXIe-6341 data acquisition card.

programming tool imitates real life instruments like oscilloscopes or multimeters. The variables, known from conventional programming, are replaced with the, so called, wires which connect the nods of the program. The data flow along the wires and are distributed to their ends. Example is shown in Fig. 11.20

We have written our own drivers for the micrometric table in LabVIEW that communicate via a RS232 port. The driver include tools for shifting the table and reading of the current position. Therefore, the measurement can be fully automatized.

In addition, the counters from the National instruments DAQ card are interfaced to LabVIEW. During the measurement, the number of counts is read for a user defined time and than written into a text file, together with the measurement time and the position of the table.

If the area scan is run instead of the single measurement, the station works as follows: The first and the last position have to be defined, together with the step length. The number of counts is measured for the defined time, as described above,

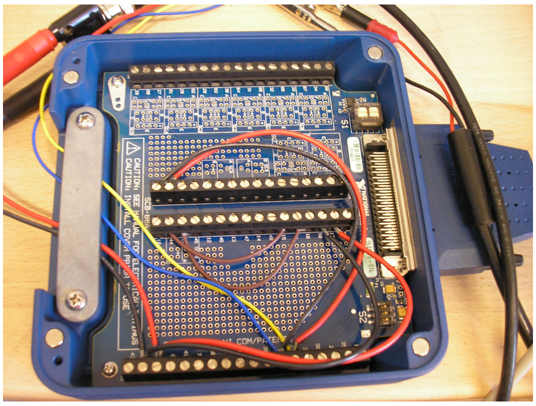

Figure 11.19: Photograph of the opened connector block. The connections inside the block (that do not lead outside) are currently redundant but they were used for the test purposes.

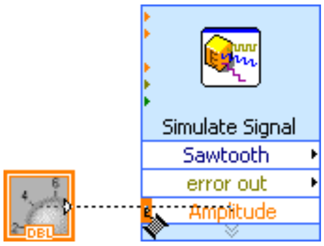

Figure 11.20: Example of the LabVIEW VI. The user controls a knob (orange square) input which adjusts the amplitude of the simulated output signal (blue rectangle). They are connected via a wire which ensures that the signal from the knob is connected to the output [86].

and than it is written into the text file. Afterwards, the table moves to the next location and measures again, etc. until the end of the scanned area is reached. In every step, the numbers of counts from the two counters, the measurement time, and the position are written into the text file. In addition it is possible to set the first step of the measurement and resume a previous one if it was stopped for some reason.

Therefore, the whole measurement is fully automatized and the operator only needs to prepare the sample, than close the dark chamber and set the voltages on the power sources. After that, the measurement is simply started with one click of the mouse. The user interface of the probing station is shown in Figure 11.21.

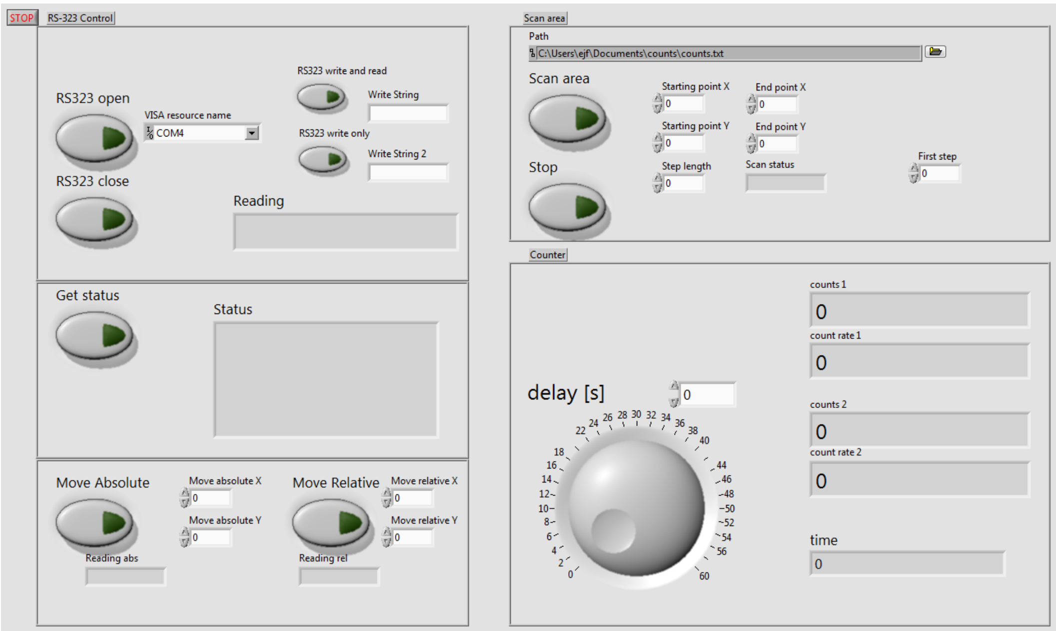

Figure 11.21: The probing station's user interface. The area on the left is dedicated to the MLC–2 micrometric table control. The area on the right is used for the supervision of the experiment.

Chapter 12

Testing of scintillator readout

The test of the optical readout from several samples was made with uncollimated radiation sources. Components from the probing station were used for the test, namely: the dark chamber, the photomultipliers, the oscilloscopes and the counter. However, the micrometric table and the collimator were not yet needed to obtain conclusive evidence.

As the radiation sources, the X-ray source described in Section 11.3, and also Am^{241} alpha source with two main energies of alpha particles: (5485.56 ± 0.12) MeV at 84.5% branching ratio (BR) and (5442.80 ± 0.13) MeV at 14% [6]. The alpha source is shown in Fig. 12.1.

Figure 12.1: Photograph of the Am^{241} alpha source.

Next, the outcome of testing of several samples will be discussed.

12.1 Sample with spherical lenses

This sample is shown in Figure 12.2: It is a previously prepared sample where two optical fibers with attached spherical lenses oppose each other. The size of the scintillator is $18 \times 7 \times 0.4$ mm^3.

Both radiation sources were used – the X-ray and alpha, however the signal was too overrun by the noise to make any conclusions from the measurement. Therefore, coincidence measurements will have to be made to obtain reasonable data.

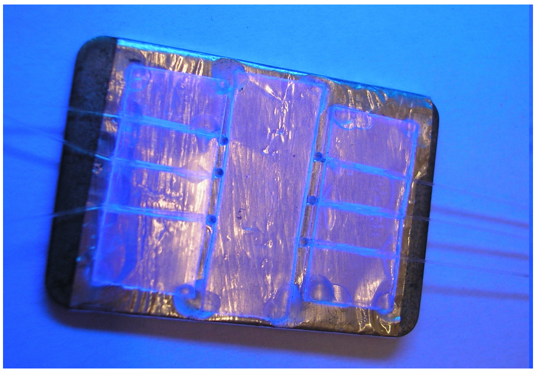

Figure 12.2: Photograph of the sample where fibers with spherical lenses face the opposite direction.

12.2 Sample with a large scintillator glued directly to a photomultiplier

In this measurement, two photomultipliers were used: one glued directly to a $35 \times 35 \times 3.5$ mm^3 scintillator, and another one where the optical fiber was read out. An optical fiber with a spherical lens was used. The scintillator, connected to the photomultiplier is shown in Figure 12.3.

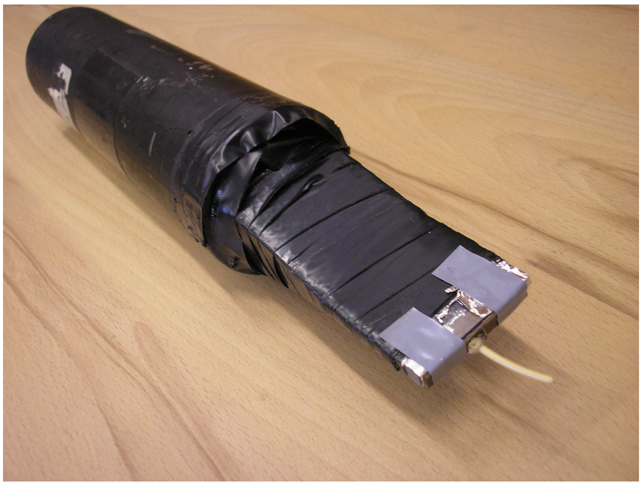

Figure 12.3: Photograph of a $35 \times 35 \times 3.5$ mm^3 scintillator glued directly to a photomultiplier. The mount for the optical fiber can be seen. The place near the optical fiber mount is bare because the alpha source was attached there.

The Am^{241} alpha source was used in this measurement. Because the alphas are monoenergetic, they create very stable signal on the directly glued photomultiplier (see Fig. 12.4).

Both photomultipliers were connected to the same oscilloscope on which the trigger was set to the alpha signal on the directly glued photomultiplier to the

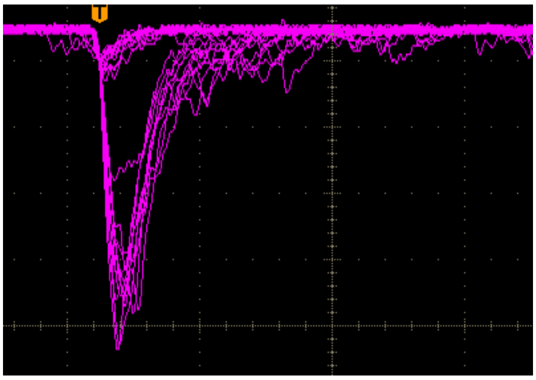

Figure 12.4: Signal in oscilloscope connected to the photomultiplier that is directly glued to a scintillator. The signal from the alphas at ≈ 80 mV can be seen, although the trigger is set to 13 mV.

signal of incoming alphas. The signal was plotted continuously so that the signal peaks overlap and are not erased. No coincidence counts were seen, however, on the fiber readout.

The height of the signal depends very much on the ratio between the cross-sectional areas of the scintillator and the optical fiber [23]. Therefore, a similar measurement was made with smaller scintillator samples.

12.3 Sample with small scintillators glued directly to a photomultiplier

For this measurement, we prepared two samples of organic scintillators $7 \times 5 \times 0.4$ mm^3. The samples were first cut with a milling cutter and than polished with a very fine emery paper and a piece of cloth. An optical fiber was glued directly to one sample via optical varnish, the other one was attached to a fiber with a spherical lens. Finally, both were glued to a photomultiplier. The samples are shown in Figure 12.5.

The same measurement layout was used as in Section 12.2. Both photomultipliers were connected to one oscilloscope and the trigger was set to the signal from the incoming alphas. The oscilloscope was set to keep all the triggered signals visible and to erase them after 0.5 s. The screenshots from the oscilloscope are shown in Figure 12.6(a) without the spherical lens and 12.6(b) with one.

In both of the samples some coincidences were observed. However, the sample with the optical fiber directly glued to the scintillator showed a lot higher coincidence count rate than the one with the spherical lens. The ratio between the height of the signal of the photomultiplier with the fiber and the directly attached one is approximately 1/60 for the scintillator without the spherical lens and 1/70 for the scintillator with one.

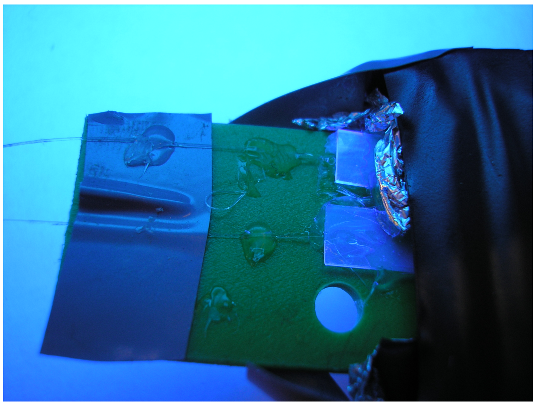

Figure 12.5: Photograph of two oscillator samples glued directly to the photomultiplier. The upper one has the optical fiber attached with a spherical lens and the bottom one without a spherical lens (but is glued to the scintillator via optical varnish).

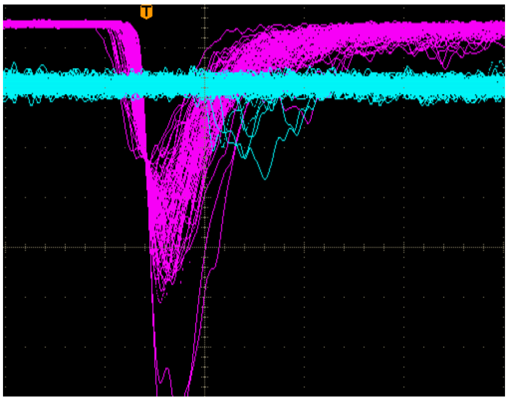

(a) Without spherical lens

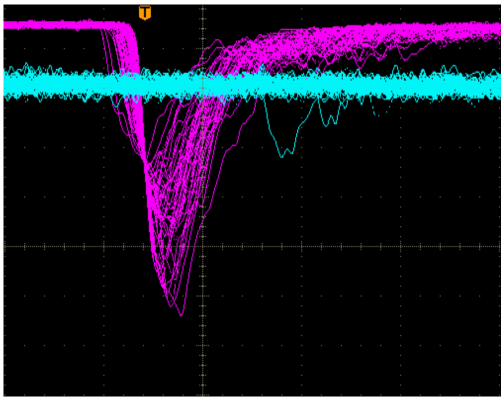

(b) With spherical lens

Figure 12.6: Screenshots of the oscilloscope output from the measurements with the small scintillator samples. The pink signal is from the directly glued photomultiplier the blue one is from the photomultiplier that reads out the optical fiber. The signal from alphas is at $\approx 60 - 70$ mV at the directly glued photomultiplier and $\approx 0.5 - 2$ mV at the one that reads out the optical fiber.

12.4 Discussion of the results

In these measurements, the readout option with the spherical lens seems like an inferior option to the one with the fibers simply glued to the scintillation pads. Therefore, at this point, the simulations in Section 10.4 are proved right.

The optical properties of all the used components are very sensitive, however, to the properties of the surface. Thus, with better refinement of the surface, the results could significantly change. Possibly, even in favor of the spherical lens option.

Another point is that without the employment of the wavelength shifters, the volume of the pads will have to be very limited. The WLS's, however, introduce other problems that will have to be tested. For example, the radiation hardness will be lowered and the physical placement at the scintillator pads will have to be investigated.

Chapter 13

Conclusion

13.1 Detector control system for the Silicon Drift Detector

The first long shutdown of the LHC (LS1) is currently under way in 2013. Therefore, several changes to the DCS, that would be otherwise impossible, were made. In addition, some faulty equipment was replaced.

Low voltage power supply cables for the SDD chips that were swapped from the beginning of the SDD operation were changed to their proper location. This was only possible because the L3 magnet was opened during the LS1.

A faulty humidity sensor and high voltage power supply racks were replaced; the HV racks because they produced slightly different voltages then they were commanded to. Both, the humidity sensor and the HV racks, will have to be tested when the cooling and ventilation are ready.

Another big problem with the HV power supply was that it started dumping commands when too many of them were issued. This may cause that in some cases a difference of voltages between two neighboring modules might well exceed 2 kV. Solutions are currently under investigation.

All of the above-listed changes should be ended until the end of the LS1. Therefore, the performance of the detector would improve greatly after the shutdown.

13.2 Scintillator version of the Forward Calorimeter FoCal

A design concept for the ALICE Forward Calorimeter with the use of scintillators as the sensitive medium is being developed at Czech Technical University. As opposed to the concept with silicon detectors, the scintillators have several advantages: they have superior radiation hardness, they do not introduce cooling and power supply into the detector area, and they cost less.

The readout of the scintillator pads is done via optical fibers. One of the features of the scintillator design that is currently under development is the interface between the scintillator pads and the optical fibers. There are essentially three design considerations for the interface: A directly glued fiber to the scintillator, a spherical lens is glued to the end of the fiber which should further the geometrical acceptance, or a wavelength shifter is either glued to one edge of the scintillator or embedded inside the scintillator volume.

To test the scintillator readout, we have built a functional probing station that is capable of automatic scanning of the whole area of detector pads via radiation and it measures the detector readout in every point of the detector volume. The station is operated from a single computer and is capable of saving the measured data into a text file.

As the probing station's source of radiation, we made an X-ray source capable of production of a collimated beam of several hundred photons. The spectra of the X-rays were measured, using a HPGe spectrometer and the geometrical properties of the beam were tested via the Medipix3 detector.

As a byproduct of the development of the probing station, a lot of laboratory equipment was put into operation and/or tested. This includes: radiation sources, photomultipliers, amplifiers, the HPGe spectrometer, and automated measurement and control tools from National Instruments. This equipment can be used for other projects or for educational purposes.

Several conclusive results were obtained by testing multiple samples for the scintillator pad design. In these measurements an uncollimated Am^{241} alpha source was used because the number of measured particles would drop severely, if a collimator was introduced.

These measurements show that the readout option with the spherical lenses is inferior to the one with the directly glued fiber. However, the surface refinement may play a crucial role in the readout efficiency and may have to be improved.

At this moment, the WLS variant of the readout seems like the most suitable option because the readout efficiency of the other two options is most probably insufficient. Pad samples with the WLS readout will have to be prepared and tested in the future.

List of Abbreviations

ACORDE .... ALICE Cosmic Ray Detector

ACR .... ALICE Control Room

BR .... Branching Ratio

CaV .... Cooling and Ventilation

CERN .... Centre Européenne pour Recherche Nucléaire (European Organization for Nuclear Research)

CGC .... Color Glass Condensate

CMOS .... Complementary Metal–Oxide–Semiconductor

CU .... Control Unit

DAQ .... Data Acquisition

DGLAP .... Dokshitzer, Gribov, Lipatov, Altarelli, Parisi

DIM .... Distributed Information Management

DIP .... Data Interchange Protocol

DP .... DataPoint

DPT .... DataPoint Type

DU .... Device Units

ECS .... Experiment Control System

EMC .... Electromagnetic Cascade

EMCal .... ElectroMagnetic CALorimeter

FERO .... Front-End Electronics and Readout

FMD .... Forward Multiplicity Detector

FoCal .... Forward Calorimeter

FWHM .... Full Width in Half Maximum

HGL .... High-Granularity Layers of FoCal

HLT .... High-Level Trigger

HMPID .... High Momentum Particle Identification Detector

HPGe .... Hyper-Pure Germanium

HV .... High Voltage

ID .... Internal Diameter

ITS .... Inner Tracking System

LEP .... Large Electron-Positron Collider

LGL .... Low-Granularity Layers of FoCal

LHC .... Large Hadron Collider

LS1 .... First long shutdown of the LHC

LS1 .... Long Shutdown 1

LU .... Logical Unit

LV .... Low Voltage

MAPS .... Monolithic Active Pixel Sensors

MCM .... Multi-Chip Module

MOS .... Metal-Oxide Semiconductor

NEG .... Non-Evaporable Getter

NI .... National Instruments

nPDF .... Nuclear Parton Distribution Function

NTD silicon ..... Neutron Transmutation Doped silicon

OPC .... Object Linking and Embedding for Process Control

PDF .... Parton Distribution Function

PHOS .... Photon Spectrometer

PLC .... Programmable Logic Controller

PMD .... Photon Multiplicity Detector

PP .... PolyPropylene

pQCD .... Perturbative QCD

QCD .... Quantum ChromoDynamics

QED .... Quantum Electrodynamics

QGP .... Quark-Gluon Plasma

SCADA .... Supervisory Controls and Data Acquisition

SDD .... Silicon Drift Detector

SPD .... Silicon Pixel Detector

SSD .... Silicon Strip Detector

T0 .... Time 0 detector

TOF .... Time-of-Flight

TPC .... Time-Projection Chamber

TRD .... Transition Radiation Detector

TRG .... Trigger System

UI .... User Interface

V0 .... Vertex 0 detector

VI .... Virtual Instrument

WLS .... WaveLength Shifter

ZDC .... Zero Degree Calorimeter

Bibliography

[1] ALICE Collaboration, *The ALICE experiment at the CERN LHC*, *JINST* 3 S08002 (2008).

[2] F. Carminati et al., *ALICE: physics performance report, volume I*, J. Phys. G 30 (2004) 1517.

[3] B. Alessandro et al., *ALICE: physics performance report, volume II*, J. Phys. G 32 (2006) 1295.

[4] ALICE collaboration, *Technical proposal for A Large Ion Collider Experiment at the CERN LHC*, CERN-LHCC-95-71, `http://cdsweb.cern.ch/record/293391`.

[5] Particle Data Group, *Review of particle properties*, Rev. Mod. Phys., Vol. 52, No. 2, Part II, (April 1980).

[6] Particle Data Group, *WWW Table of Radioactive Isotopes*, `http://ie.lbl.gov/toi/index.asp` (cit. July 27, 2013).

[7] ALICE collaboration, *ALICE Inner Tracking System (ITS): Technical Design Report*, CERN-LHCC-99-012, `http://edms.cern.ch/file/398932/1`.

[8] ALICE collaboration, *ALICE trigger data-acquisition high-level trigger and control system: Technical Design Report*, CERN-LHCC-2003-062, `http://cdsweb.cern.ch/record/684651`.

[9] *Official web pages of the ALICE DCS*, `http://alicedcs.web.cern.ch/alicedcs/`, (cit. July 15, 2013).

[10] J. Král, *Research project*, Faculty of Nuclear Sciences and Physical Engineering, Czech Technical University in Prague, Prague (2007).

[11] ETM company, *PVSS information for newcomers*, `http://lhcb-online.web.cern.ch/lhcb-online/ecs/PVSSIntro.htm`, (cit. August 24, 2013).

[12] *JCOP*, `http://itco.web.cern.ch/itco/Projects-Services/JCOP/welcome.html`, (cit. August 24, 2013).

[13] *JCOP Documentation*, `http://j2eeps.cern.ch/wikis/display/EN/JCOP+Framework+Documentation`,

(cit. July 15, 2013).

[14] P.C. Burkimsher, *JCOP experience with a commercial SCADA product PVSS, Proceedings of the ICALEPCS 2003*, Gyeongju Korea (2003), http://cdsweb.cern.ch/record/924942.

[15] A. Daneels and W. Salter, *Selection and evaluation of commercial SCADA systems for the controls of the Cern LHC experiments, Proceedings of the ICALEPCS99 conference*, Trieste Italy (1999), http://cdsweb.cern.ch/record/532627.

[16] B. Briss, M. Schagginger, L. Knipp, *PVSS II getting started*, (2004), http://j2eeps.cern.ch/wikis/download/attachments/14778428/0407PVSS_II_GettingStarted_Basics_en.pdf?version=1&modificationDate=1299054760000.

[17] D. Brand and P. Zafiropulo, *On Communicating Finite-State Machines*, Journal of the Association for Computing Machinery Vol 30 No 2 (1983) 323.

[18] A. Daneels and W. Salter, *What is SCADA?, Proceedings of the ICALEPCS99 conference*, Trieste Italy (1999), https://accelconf.web.cern.ch/accelconf/ica99/papers/mc1i01.pdf.

[19] The OPC Foundation, *About OPC*, http://www.opcfoundation.org/Default.aspx/01_about/01_whatis.asp (cit. July 15, 2013).

[20] ETM company, *PVSS – DIM Integration*, http://lhcb-online.web.cern.ch/lhcb-online/ecs/fw/FwDim.html (cit. July 15, 2013).

[21] M. Sitta, *The Silicon Drift Detector of the ALICE experiment*, Nucl. Instrum. Meth. A 611 (2010) 591.

[22] A. Morsch and B. Pastircak, *Radiation in ALICE detectors and electronic racks*, ALICE Internal Note ALICE-INT-2004-017, http://edms.cern.ch/file/358706/1.

[23] D. Green, *The Physics of Particle Detectors*, Cambridge University Press, New York (2000).

[24] J. Gerndt and P. Průša, *Detektory ionizujícího záření*, Vydavadelství ČVUT, Prague (2011).

[25] J. Hladký, *Detektory, systémy detektorů a aparatury pro fyziku částic*, Institute of Physics ASCR, Prague (1996).

[26] D. Nouais et al., *The ALICE silicon drift detector system*, Nucl. Instrum. Meth. A 501 (2003) 119, ALICE-PUB-2001-59, http://cdsweb.cern.ch/record/531804.

[27] F. Antinori et al., *Experience with a 30 cm^2 silicon pixel plane in CERN experiment WA97*, Nucl. Instrum. Meth. A 360 (1995) 91.

[28] A. Rashevsky et al., *Characteristics of the ALICE Silicon Drift Detector*, Nucl. Instrum. Meth. A 461 (2001) 133.

[29] The ALICE FoCal Collaboration, A FoCal for the ALICE experiment, Letter of Intent (2012).

[30] C.W. Fabjan, *Calorimetry in High-energy Physics*, in: Experimental Techniques in Nuclear and Particle Physics, T. Ferbel ed., World Scientific, (1991).

[31] C.W. Fabjan and T.Ludlam, *Calorimetry in High-Energy Physics*, Ann. Rev. Nucl. Part. Sci. 32 (1982), reprinted in Formulae and Methods in Experimental Data Evaluation, R.K. Bock ed., European Physical Society 1984.

[32] S.W. Moser, W.F. Harder, C.R. Hurlbut, and M.R. Kusner, *Principles and Practice of Plastic Scintillator Design*, Radiat. Phys. Chem.: 31–36 (1993).

[33] S. Eidelman et al., *Review of Particle Physics: Passage of Particles through matter*, Phys. Let. B, Vol. 592 (2004) 1.

[34] E. Longo and I. Sestili, *Monte Carlo calculation of photon-initiated electromagnetic showers in lead glass*, Nucl. Instr. Meth. 2, Vol. 128 (1975) 283.

[35] D.I. Sober et al., *An experimental study of photon-initiated showers in lead between 150 and 450 MeV*, Nucl. Instr. Meth., Vol. 73 (1969) 29.

[36] G. Bathow, E. Freytag, K. Tesch, *Measurements on 6.3 GeV electromagnetic cascades and cascade-produced neutrons*, Nucl. Phys. B, Vol. 2 (1967).

[37] T. Yuda, *Electron-induced cascade showers in inhomogeneous media*, Nucl. Instr. Meth., Vol. 73 (1969).

[38] H. Göringer, H.J. Von Eyß, B. Schoch, *Measurement of photon showers in lead produced by electrons of 150 MeV*, Nucl. Instr. Meth., Vol. 138 (1976).

[39] G. Altarelli, G. Parisi, *Asymptotic freedom in parton language*, Nucl. Phys. B126 (1977) 298.

[40] J.C. Collins, D.E. Soper, G. Sterman, *Factorization of Hard Processes in QCD*, Adv. Ser. Direct. High Energy Phys. 5, 1 (1988), arXiv:hep-ph/0409313.

[41] R.D. Ball et al. (NNPDF collaboration), *Unbiased global determination of parton distributions and their uncertainties at NNLO and at LO*, Nucl. Phys. B 849 (2011) 296.

[42] L. McLerran and R. Venugopalan, *Gluon distribution functions for very large nuclei at small transverse momentum*, Phys. Rev. D 49 (1994) 3352–3355.

[43] A. Kovner, L. McLerran and H. Weigert, *Gluon Production at High Transverse Momentum in the McLerran-Venugopalan Model of Nuclear Structure Functions*, School of Physics and Astronomy, University of Minnesota, Minneapolis (1995), arXiv:hep-ph/9505320.

[44] The European Muon Collaboration, *The ratio of the nucleon structure functions F_2^N for iron and deuterium*, Phys. Lett. 123 B (1983) 275.

[45] C.A. Salgado, *The physics potential of proton–nucleus collisions at the TeV scale*, J. Phys. G 38 (2011) 124036.

[46] Y. Hori, H. Hamagaki and T. Gunji, *Simulation study for Forward Calorimater in LHC-ALICE experiment*, J. Phys.: Conf. Ser. 293 (2011), doi:10.1088/1742-6596/293/1/012029.

[47] S. Muhuri and T.K. Nayak, *Simulation and design studies of ALICE Forward Calorimeter*, Proceedings of the DAE Symp. on Nucl. Phys. 57 (2012).

[48] University of Bergen FoCal group's wiki page, `https://wikihost.uib.no/ift/index.php/FOCAL_-_Forward_Calorimeter` (cit. July 15, 2013).

[49] Private conversations with Doc. RNDr. Vojtěch Petráček CSc.

[50] R. Lavička, *Bachelor Thesis: Studie dopředného elektromagnetického kalorimetru pro experiment ALICE*, Faculty of Nuclear Sciences and Physical Engineering, Czech Technical University in Prague, Prague (2013), `http://physics.fjfi.cvut.cz/publications/BP_Roman_Lavicka.pdf`.

[51] J. Sasínek, *Bachelor Thesis: Dopředný elektromagnetický kalorimetr pro experiment ALICE*, Faculty of Nuclear Sciences and Physical Engineering, Czech Technical University in Prague, Prague (2013).

[52] D. B. Oliver and G. F. Knoll, *Anisotropy of Scintillation Response of Anthracene to Neutron Generated Recoil Protons and Carbon Ions*, IEEE Trans. Nucl. Sci. NS-15(3) (1968) 122.

[53] F. Markley et al., *Development of Radiation Hard Scintillators*, Radiat. Phys. Chem., Vol. 41 (1993) 135.

[54] G. Marini et al., *Radiation Damage to Organic Scintillation Materials*, CERN Pub. 85-08, Geneva (1985).

[55] A.D. Brass and A. Pla-Dalmau, *Radiation Effects in Plastic Scintillators and Fibers*, FERMILAB-PUB-91-74 (1991).

[56] C. Zorn et al., *Results of a Low Dose Rate Irradiation of Selected Plastic Scintillating Fibers*, IEEE Trans. Nucl. Sci. 37(2) (1990) 487.

[57] A.D. Brass and A. Pla-Dalmau, *Radiation-Induced Polystyrene Hidden Absorption Effects in Based Plastic Scintillator*, FERMILAB-PUB-90/224 (1990).

[58] K.F. Johnson et al., *High Dose Calorimetry with Scintillating Fibers*, IEEE Trans. Nucl. Sci. 37(2) (1990) 500.

[59] A.D. Brass and A. Pla-Dalmau, *Radiation Effects in Intrinsic 3HF Scintillator*, FERMILAB-PUB-92/247 (1992).

[60] S.W. Han et al., *Radiation Hardness of 3HF-Tile/02-WLS-Fiber Calorimeter*, FERMILAB-TM-1865 (1993).

[61] Private conversations with Roman Lavička.

[62] F.X. Gentit, *SLitrani web pages*, http://gentitfx.fr/SLitrani/ (cit. July 24, 2013).

[63] F.X. Gentit, *Optics inside anisotropic media*, http://gentitfx.fr/litrani/birefringence/Physics_behind.pdf (cit. July 24, 2013).

[64] J. Chýla, *Quarks, partons and Quantum Chromodynamics*, Institute of Physics, Academy of Sciences of the Czech Republic, Prague (2007).

[65] F. Halzen and A.D. Martin, *Quarks and Leptons: An Introductory Course in Modern Physics*, J. Wiley & Sons Inc., New York (1984).

[66] W. Greiner, S. Schramm, E. Stein, *Quantum Chromodynamics*, 3rd Revised and Enlarged Edition, Springer, New York (2007).

[67] T. Kamon, K. Kondo, A. Yamashita, *A new scintillator and wavelength shifter*, Nucl. Instr. Meth. 213 (1983) 261.

[68] FastVision LLC., *FastCamera13*, http://fast-vision.com/index.php?submenu=cameras&src=gendocs&ref=FastCamera13&category=cameras, (cit. July 24, 2013).

[69] FastVision LLC., *FastCamera13 User's manual*, Nashua USA (2004).

[70] Photobit Corporation, *PB-MV13 20mm CMOS Active-Pixel Digital Image Sensor*, http://fast-vision.com/clientuploads/PDFs/PB-MV13_Product_Specification.pdf (cit. July 24, 2013).

[71] LANG GMBH & CO., *Precision positioning system MCL*, http://forums.ni.com/ni/attachments/ni/140/42418/1/MCL%20Manual.pdf (cit. July 26, 2013).

[72] TECHNIX company, *Operator Manual: SR100-P-300 Model*, Créteil, France (2012).

[73] Spellman corporation, *225 Series User's Manual*, http://www.spellmanhv.com/~/media/Files/Technical-Resources/Manuals/225MAN.ashx (cit. July 25, 2013).

[74] *Zdroj rentgenového záření s DY 87*, http://danyk.cz/rtg.html (cit. July 25, 2013).

[75] Philips, *DY 86, DY 87 Single Anode E.H.T. Rectifying Tubes*, http://frank.pocnet.net/sheets/010/d/DY86.pdf (cit. July 25, 2013).

[76] Medipix collaboration, *Medipix home page*, http://medipix.web.cern.ch/medipix/index.php (cit. July 25, 2013).

[77] R. Ballabriga et al., *The Medipix3 Prototype, a Pixel Readout Chip Working in Single Photon Counting Mode With Improved Spectrometric Performance*, IEEE Trans. Nucl. Sci. NS-54 (2007) 1824.

[78] Tektronix, Inc., *DPO4000 Series Digital Phosphor Oscilloscopes User Manual*, http://www.tequipment.net/pdf/tektronix/DPO4000_UserManual.pdf (cit. July 26, 2013).

[79] Tektronix, Inc., *Digital Phosphor Oscilloscopes DPO4000 Series Datasheet*, http://www.tequipment.net/pdf/tektronix/DPO4000_datasheet.pdf (cit. July 26, 2013).

[80] RIGOL Technologies, Inc., *DS4000 Series Digital Oscilloscope User's Guide*, UGA10105-1110 (2011).

[81] National Instruments, *NI PXIe-1078 9-Slot 3U PXI Express Chassis With AC - Up to 1 GB/s*, http://sine.ni.com/nips/cds/print/p/lang/cs/nid/209253 (cit. July 26, 2013).

[82] National Instruments, *Laptop Control of PXI (ExpressCard MXI for PXI Express) NI PXIe-ExpressCard8360, NI ExpressCard-8360, NI PXIe-8360*, http://www.ni.com/pdf/products/us/cat_pxie8360.pdf (cit. July 26, 2013).

[83] National Instruments, *NI PXI-8432/2 (RS232) High-Performance, Isolated 2-Port Serial Interface for PXI*, http://sine.ni.com/nips/cds/print/p/lang/cs/nid/203604 (cit. July 26, 2013).

[84] National Instruments, *NI PXIe-6341 X Series Data Acquisition*, http://sine.ni.com/nips/cds/print/p/lang/cs/nid/207415 (cit. July 26, 2013).

[85] National Instruments, *NI PXIe-6341 Manuals*, http://sine.ni.com/nips/cds/nisearchservlet?nistype=psrelcon&nid=207415&lang=cs&q=FQL:((nilangs:en))%20AND%20((phwebnt:11512))%20%20AND%20(nicontenttype:productmanual)%20AND%20(docstatus:current)RANK%20nilangs:en&title=NI%20PXIe-6341%20Manuals (cit. July 26, 2013).

[86] National Instruments, *Getting Started with LabVIEW*. http://www.ni.com/pdf/manuals/373427h.pdf (cit. July 26, 2013).

[87] M. Šimko, *Bachelor Thesis: Detector Control System for the ALICE Experiment*, Faculty of Nuclear Sciences and Physical Engineering, Czech Technical University in Prague, Prague (2011), http://ejcf.fjfi.cvut.cz/publications/BP_Miroslav_Simko.pdf.

[88] M. Šimko, *Research Project: Detector Control System for the ALICE Experiment*, Faculty of Nuclear Sciences and Physical Engineering, Czech Technical University in Prague, Prague (2012), http://ejcf.fjfi.cvut.cz/publications/VU_Miroslav_Simko.pdf.